



CHALMERS
UNIVERSITY OF TECHNOLOGY



Effect of Fuel Cell Operating Potential Window on Pt/C Catalyst Durability

Master's thesis in Materials Chemistry

ASTRID HJERN

DEPARTMENT OF PHYSICS

CHALMERS UNIVERSITY OF TECHNOLOGY
Gothenburg, Sweden 2023
www.chalmers.se

MASTER'S THESIS 2023

Effect of Fuel Cell Operating Potential Window on Pt/C Catalyst Durability

ASTRID HJERN



CHALMERS
UNIVERSITY OF TECHNOLOGY

Department of Physics
Division of Chemical Physics
CHALMERS UNIVERSITY OF TECHNOLOGY
Gothenburg, Sweden 2023

Effect of Fuel Cell Operating Potential Window on Pt/C Catalyst Durability
ASTRID HJERN

© ASTRID HJERN, 2023.

Supervisor: Marika Männikkö, PowerCell Group AB
Examiner: Björn Wickman, Department of Physics

Master's Thesis 2023
Department of Physics
Division of Chemical Physics
Chalmers University of Technology
SE-412 96 Gothenburg
Telephone +46 31 772 1000

Cover: Pt/C coating on a glassy carbon electrode.

Typeset in L^AT_EX
Printed by Chalmers Reproservice
Gothenburg, Sweden 2023

Abstract

The proton exchange membrane fuel cell is a potential key player in reducing greenhouse gas emissions. There is, however, a need for further improvements in Pt on carbon support catalyst (Pt/C) durability and costs. The purpose of this thesis is to improve catalyst durability by investigating what upper potential limit (UPL) voltage clipping should be implemented during load cycling. It is further investigated how scan rate affects catalyst durability. Based on previous research, possible causes and pathways of Pt degradation are discussed. Three catalysts from different producers with varying support surface area are examined with accelerated stress tests (ASTs) using triangular wave . One AST was performed with a scan rate of 250 mV/s in the potential window of 0.6 to 1.0 V. Four ASTs were performed with a scan rate of 50 mV/s with a set lower potential limit (LPL) of 0.6 and varying UPL between 0.7-1.0 V. The electrochemical surface area (ECSA) is calculated to track catalyst degradation at specific intervals during the ASTs.

The degradation of the catalyst increases with a higher scan rate from 23 to 26% for scan rates of 50 mV/s and 250 mV/s, respectively. All three catalysts show a decrease in degradation when the UPL is lowered from 1.0 to 0.8 V. With decreased UPL a thinner oxide layer is formed. The degradation increases for two catalysts at UPL 0.7, possibly due to error sources in the method. The Pt/C catalyst with a support area of 750 m²/g displayed the lowest degradation possibly due to a large inter-particle distance. The primary degradation mechanisms for platinum in the potential window of 0.6 and 1.0 V are commonly described as Pt dissolution and agglomeration. Based on the results, it can be concluded that a decreasing UPL in the region 1.0 to 0.8 V and increasing support area results in lower catalyst degradation. However, the influence of initial ECSA variations, low coating quality, and ink age questions the accuracy of the results. Therefore, it would be beneficial to repeat the current tests with a more controllable method.

Keywords: Proton exchange membrane fuel cell, accelerated stress test, triangular wave, electrochemical surface area, rotating disk electrode, upper potential limit, scan rate, Pt/C.

Acknowledgements

I would like to thank PowerCell Group AB for giving me the opportunity to perform my master's thesis in the R&D lab, as well as my colleagues for cheering me on throughout the process. I am grateful to my supervisor Marika Männikkö for her feedback and discussion during this thesis. Special thanks go to Lorena Balint who assisted with the experimental part. Furthermore, I would like to thank Gabor Toth and Xiaoling Jiang for sharing knowledge and interesting discussions on our weekly catalyst meetings. Finally, I would like to thank my examiner Björn Wickman for keeping me on track and supporting me during the completion of the thesis.

Astrid Hjern, Gothenburg, June 2023

List of Acronyms

Below is the list of acronyms that have been used throughout this thesis listed in alphabetical order:

AST	Accelerated Stress Test
BET	Brauner, Emmett, Teller
GCB	Graphitized Carbon Black
GDL	Gas Diffusion Layer
CV	Cyclic Voltammetry
DOE	Department of Energy
ECSA	Electrochemical Surface Area
HSAC	High Surface Area Carbon
HOR	Hydrogen Oxidation Reaction
LPL	Lower Potential Limit
MEA	Membrane Electrode Assembly
PEMFC	Proton Exchange Membrane Fuel Cell
Pt/C	Platinum on Carbon Support
Pt	Platinum
ORR	Oxygen Reduction Reaction
RDE	Rotating Disk Electrode
RHE	Reversible Hydrogen Electrode
UN	United Nations
UPL	Upper Potential Limit

Contents

List of Acronyms	ix
List of Figures	xiii
List of Tables	xv
1 Introduction	1
1.1 Project Aim	2
1.2 Demarcation	2
2 Theory	3
2.1 Proton Exchange Membrane Fuel Cell	3
2.2 Carbon Support	5
2.3 Degradation Mechanisms	6
2.3.1 The Proximity Effect	9
2.4 Rotating Disk Electrode	9
2.4.1 Cyclic Voltammetry	10
2.4.1.1 Electrochemical Surface Area	11
2.4.2 Accelerated Stress Tests	11
3 Experimental	13
3.1 Catalysts	13
3.2 Ink Preparation	13
3.3 RDE Preparation	15
3.4 Accelerated Stress Test	16
4 Results and Discussion	21
4.1 Scan Rate	21
4.2 Upper Potential Limit	22
4.2.1 Catalyst A	22
4.2.2 Catalyst B	24
4.2.3 Catalyst C	25
4.2.4 Comparison of Catalyst A, B, and C	26
4.3 Support Material	29
4.4 Accuracy of Method	30
4.4.1 ECSA variations	30
4.4.2 Conditioning Scans	32

5	Conclusions	33
5.1	Outlook	34
	Bibliography	37
A	Appendix 1	I

List of Figures

2.1	Schematic image of the membrane electrode assembly for a PEMFC. Consisting of GDL, anode, membrane, and cathode. In addition the mass transport pathways are presented.	3
2.2	Illustrations of known common degradation mechanisms in fuel cells such as Pt agglomeration, Pt dissolution, carbon corrosion, and Pt detachment. Black box symbols are carbon support and white spheres are Pt atoms.	6
2.3	The place-exchange mechanism illustrates the Pt oxide layer formation and Pt oxide dissolution in the anodic and cathodic scans. The white, red, and blue sphere represents Pt, oxygen, and hydrogen atoms, respectively.	7
2.4	Cyclic voltammogram with current (A) vs potential (V). The blue region represents the hydrogen adsorption area is integrated to produce Q_{HUPD}	10
2.5	Cycle profiles square, triangular and asymmetrical triangular in the potential interval 0.6 – 1.0 V. Red is the anodic scan and green is the cathodic scan.	12
3.1	A clean GC electrode emerged in PEEK used for ASTs.	14
3.2	Assembled and connected RDE cell to potentiostat with reference, working, and counter electrode emerged in the electrolyte of 0.1 M HClO ₄	15
4.1	Average degradation for Catalyst A with an UPL 1.0 V for scan rate 250 (light blue) and 50 (dark blue) mV/s up to 17.78 h of potential cycling. The standard deviation and average is calculated from three repetitions.	21
4.2	ECSA (m ² /g) over time (h) for Catalyst A, ink 1 at UPL 1.0 (dark blue), 0.9 (purple), 0.8 (light blue), and 0.7 (orange) V up to 17.78 h with a scan rate of 50 mV/s. Each UPLs has three repetitions.	23
4.3	Average ECSA loss (%) over time (h) for Catalyst A, ink 1 at UPLs 1.0 (dark blue), 0.9 (purple), 0.8 (light blue), and 0.7 (orange) V up to 17.78 h a scan rate of 50 mV/s. The average and standard deviation is based on three repetitions.	23

4.4	ECSA (m^2/g) over time (h) for Catalyst B, ink 2 (solid line) and 3 (dashed line) at UPLs 1.0 (dark blue), 0.9 (purple), 0.8 (light blue), 0.7 (orange) V up to 17.78 h with a scan rate of 50 mV/s. Each UPLs has three repetitions.	24
4.5	ECSA loss (%) over time (h) for Catalyst B, ink 2 (solid line) and 3 (dashed line) at UPLs 1.0 (dark blue), 0.9 (purple), 0.8 (light blue), and 0.7 (orange) V up to 17.78 h with a scan rate of 50 mV/s. The average and standard deviation is based on three repetitions.	25
4.6	ECSA (m^2/g) over time (h) for Catalyst C, ink 4 (solid line) and 5 (dashed line) at UPLs 1.0 (dark blue), 0.9 (purple), 0.8 (light blue), 0.7 (orange) V up to 17.78 h with a scan rate of 50 mV/s. Each UPLs has three repetitions.	25
4.7	ECSA loss (%) over time (h) for Catalyst C, ink 4 and 5 at UPLs 1.0 (dark blue), 0.9 (purple), 0.8 (light blue), 0.7 (orange) V up to 17.78 h with a scan rate of 50 mV/s. The average and standard deviation is based on three repetitions. The average and standard deviation is based on three repetitions.	26
4.8	Average total ECSA loss (%) of Catalyst A (yellow), B (red) and C (green) at UPLs 1.0, 0.9, 0.8, 0.7 V at 17.78 h with a scan rate of 50 mV/s. The average and standard deviation are from 3 repeated tests for each potential limit.	27
4.9	Average absolute total ECSA loss (m^2/g) for Catalyst A (yellow), B (red) and C (green) at UPL of 1.0, 0.9, 0.8, 0.7 V at 17.78 h with a scan rate of 50 mV/s. The average and standard deviation are from three repeated tests for each potential limit.	28
4.10	Average total degradation in (%) for catalysts A, B, and C at UPLs of 1.0 (dark blue), 0.9 (purple), 0.8 (light blue), and 0.7 (orange) V at 17.78 h with a scan rate of 50 mV/s.	29
4.11	Microscope images of six coatings that are used for ASTs. a) ink 1 with Catalyst A, b) ink 1, Catalyst A, c) ink 2, catalyst B, d) ink 3, catalyst B, e) ink 4, catalyst C, f) ink 5, catalyst C.	31
4.12	Total ECSA loss (%) of catalyst A and B for AST-5 in the potential window 0.6 – 0.7 V (orange) and for adjusted AST-5 with conditioning and ECSA scans at BoL and 17.78 h (blue). The error bars show the standard deviation, based on three repetitions.	32
A.1	Cyclic voltammogram current (A) over Potential (V) for catalyst C ink 5, 0.04-1.2 V with a scan rate of 20 mV/s. Green is the cyclic voltammogram at time 0 h and red is at time 17.78 h. There is an increase in the anodic scan in the interval 1.0 to 1.2 V. The cause is unknown.	I

List of Tables

3.1	Characteristics of catalysts investigated such as Pt size, support material, and support BET. Analysis techniques for determining particle size and carbon support area are not specified.	13
3.2	The compositions of the inks used for ASTs.	14
3.3	ASTs performed for catalyst evaluation.	16
3.4	The schedule for AST-1. Scan rate, the number of cycles, LPL, and UPL is specified for the conditioning and procedure scans.	17
3.5	The schedule for AST-2. Scan rate, the number of cycles, LPL, and UPL is specified for the conditioning and procedure scans.	17
3.6	The schedule for AST-3. Scan rate, the number of cycles, LPL, and UPL is specified for the conditioning and procedure scans.	18
3.7	The schedule for AST-4. Scan rate, the number of cycles, LPL, and UPL is specified for the conditioning and procedure scans.	18
3.8	The schedule for AST-5. Scan rate, the number of cycles, LPL, and UPL is specified for the conditioning and procedure scans.	19
3.9	The schedule for AST-5 adjusted. Scan rate, the number of cycles, LPL, and UPL is specified for the conditioning and procedure scans.	19
4.1	The inter-particle distance $I_{p_{ee}}$ has been calculated for catalysts A, B, and C according to Equation 2.11 with the parameters Pt loading (wt%), particle size (nm), and BET area (m^2/g) retrieved from the supplier.	30
4.2	Average and standard deviation ECSA (m^2/g) at BoL. The number of experiments for the determination of average and standard deviation is denoted as n.	31

1

Introduction

An energy transition from fossil fuels to renewable energy is necessary to reach the UN objective of limiting global warming to less than 2 °C [1]. Fuel cells have emerged as energy converters from chemically stored energy to electrical energy for automotive, marine, stationary energy storage, and aviation [2]. The energy is stored in the form of hydrogen, methanol, ethanol, or synthesis gas and then converted by a fuel cell. These fuels have the potential to be derived from renewable energy and raw materials. However, there are still challenges to implementing fuel cells in our society.

Integrating fuel cells into our society has several environmental improvements. Firstly, most of the emissions from a hydrogen fuel cell are water [3]. This will therefore improve the air quality in urban areas. Furthermore, replacing combustion engines with fuel cells will reduce greenhouse gas emissions. However, it is important to consider the whole fuel cycle. Today hydrogen is produced from fossil fuels and therefore there is little gain in terms of emissions. The aim in the future is to increase hydrogen production from renewable sources. Secondly, hydrogen fuel cells have a higher energy efficiency than combustion-based engines. For a gasoline internal combustion engine system, the efficiency at its most favourable point is 34%, and for a diesel engine about 40%. In comparison, a fuel cell system has at its most favourable point an efficiency of 50%. However, the comparison can be complex because gasoline and diesel engines have it most favourable point near maximum. Fuel cells most favourable point is at partial load which is the point where automotive engines operate most frequently. Thirdly, the simplistic design based on layer-on-layer of repetitive components and more cells equals an increase in power output. This could reduce production costs, making fuel cells a competitive energy converter.

Large investments in hydrogen infrastructure and the production of renewable hydrogen are necessary. As of 2023, there are only five refuelling stations in Sweden offering hydrogen. Another challenge for fuel cells is the durability and cost of the catalyst and ionomer. Platinum (Pt) is frequently used as a catalyst in fuel cells. The US Department of Energy (DOE) has set targets for automotive durability to 8 000 h with a 10% activity loss by the year 2050 [4]. As of 2020, the status for durability is 5 000 h with 10% in activity loss. Therefore, research should be directed into decreasing Pt agglomeration, Pt dissolution, carbon support corrosion, and membrane degradation to meet these targets. Material costs for fuel cells are closely connected to the Pt catalyst. High production volumes of fuel cells, could further inflate the price of Pt and make it necessary to replace Pt or use alloyed

catalysts. Considerable effort has been put into reducing the Pt loading in the catalyst layer. Since the 1990s the catalyst loading has decreased from 28 to 0.4 mg/cm² [2]. The durability of the catalyst can be improved by the development of more durable materials or by optimizing the operation conditions to avoid certain conditions that cause degradation [5]. One possible improvement is utilizing voltage clipping. Voltage clipping avoids the cell and catalyst exposure to high voltages which would reduce its durability. Toyota has for their commercial fuel cell automotive Mirai, implemented voltage clipping at 0.9 V [5]. Reducing cost and increasing the durability of the catalyst make fuel cells a possible replacement for combustion engines in our society.

1.1 Project Aim

The aim of this project is to improve Pt catalyst durability. This project focuses on investigating where voltage clipping at the upper potential limit (UPL) should be implemented on different catalysts through accelerated stress tests (ASTs). Throughout the project, ASTs with varying potential windows are used to investigate the UPL influence on the catalysts durability. In particular, the influence of the support area on the catalyst durability with varying UPL is examined. Other specifications such as particle size, distribution, ink, and coating preparations are discussed. In addition, possible degradation mechanisms that cause the decline in catalyst durability are considered in conjunction with literature.

Several ASTs are utilized in literature to target specific operation modes and degradation mechanisms. Therefore, the effect of electrolyte, cycle profile, and scan rate are factors that are analysed. Furthermore, the translatability between the ex-situ test method used in this project and from the in-situ method is taken into account.

1.2 Demarcation

This project only investigates the catalyst durability through ex-situ testing using a rotating disk electrode (RDE) in HClO₄ during load cycling with the inert gas of N₂. The other operation conditions idling, start/stop operation, and high load are not investigated. The catalyst mass activity (A/mg_{Pt}) and specific activity (A/cm²) which are other important parameters in the catalyst activity are not examined. A lower potential window (LPL) is not investigated. The proposed degradation mechanism that cause the catalyst degradation is not verified against any experiments using inductively coupled plasma mass spectrometer (ICP-MS), transmission electron microscopy (TEM), secondary electron microscopy (SEM), or quartz crystal microbalance (QCM).

2

Theory

2.1 Proton Exchange Membrane Fuel Cell

A proton-exchange membrane fuel cell (PEMFC) is a promising fuel cell candidate by operating at ambient temperatures, with high electrical efficiency, power density, and durability [2]. The PEMFC consist of a membrane electrode assembly (MEA), illustrated in Figure 2.1. MEAs include an anode and cathode, a proton-conducting membrane, and gas-diffusion layers (GDL).

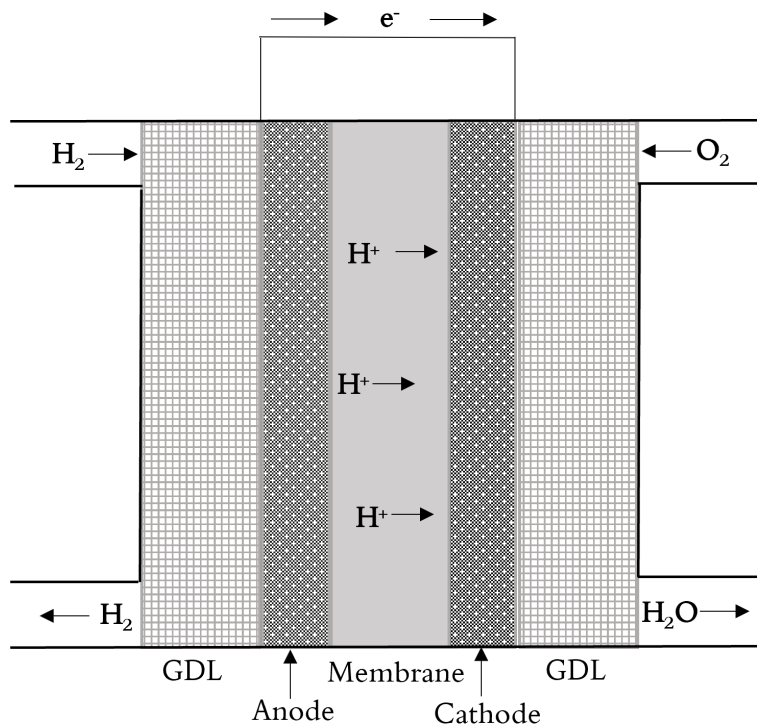


Figure 2.1: Schematic image of the membrane electrode assembly for a PEMFC. Consisting of GDL, anode, membrane, and cathode. In addition the mass transport pathways are presented.

The anode and cathode are also referred to as the catalyst layers. A catalyst decreases the activation energy for a reaction. The electrochemical reaction occurs on the catalyst surface. Therefore, the catalyst layers are thin to utilise as much catalyst as possible and reduce transport issues. On the anode, the hydrogen is

oxidised according to the hydrogen oxidation reaction (HOR) presented in Reaction 2.1.



The hydrogen proton then travels through the proton-conducting membrane to the cathode where oxygen is reduced and reacts with the hydrogen protons to produce water according to Reaction 2.2. This reaction is referred to as the oxygen reduction reaction (ORR).



The overall reaction for both the anode and cathode is presented in Reaction 2.3.



The catalyst reaction occurs on a three-node point with Pt particle, ionomer and in a void [3]. The catalyst is in general Pt with a particle size of 1 – 10 nm and placed on a carbon support. The carbon supports surface area is referred to as the BET value and is in the size range of 75 – 800 m²/g. Smaller particles size increase the catalytic activity. The high surface area of the carbon support could disperse the Pt particles more thoroughly. Therefore, in addition, generate a higher catalytic activity.

The anode and cathode are separated by a membrane layer. The membrane is a copolymer consisting of tetrafluorethylene and perfluorosulfonate monomers. Commonly used membrane materials are NafionTM, FumionTM, and FlemionTM. The membrane is often referred to as the ionomer because the side chains are ionically bonded. The sulphonic side chains are hydrophilic whereas the backbone is hydrophobic. The hydrophilic side chain could have up to 50% water uptake. In these parts, the hydrogen proton travels through from the anode to the cathode.

The electrodes and membrane are placed between a carbon layer known as GDL. Commonly used GDL are carbon fibre paper or woven fibres. It consists of pathways that distribute gas such as air/O₂, and H₂ to the electrodes. Moreover, the pathways are used to remove the water produced at the cathode. When the catalytic reaction occurs heat is generated and the GDL removes the heat that could affect the catalyst performance and durability. GDL give the MEA mechanical support and completes the full circuit for the electrons to travel through. Therefore, GDL should have good electrical and thermal conductivity, be porous to allow gases to easily and evenly travel through, and be rigid but still allow sufficient electrical contact with the electrodes.

2.2 Carbon Support

In fuel cells, Pt on carbon-based support (Pt/C) is the most commonly used catalyst. The carbon support has a large influence on the performance and durability of the fuel cell catalyst [6]. Key requirements of the support are high surface area to allow a uniform dispersion of Pt particles, low reactivity in both dry and humid environments up to 150 °C, high electrochemical stability under fuel cell operating conditions, high electronic conductivity, and easy separation of Pt from the carbon to enable recycling. The interaction between the Pt and support depends on the functional group that is present at the interface. The connection of the Pt and support is the formation of coordination bonds between the π bond on the carbon support and d-orbitals on the Pt particles. By altering the carbon support structure and therefore changing the Pt/C interaction, the durability of Pt/C can be improved.

The interactions between the support and Pt are divided into two classes, electronic and geometric. Electronic effects include the electron interactions between the Pt particles and the support. A strong interaction occurs from an overlap of the π -orbitals on the carbon support and d-band on the Pt. The overlap can be either electron-donating or accepting. Subsequently, this will alter the Pt surface electron density. By changing the surface electron density the adsorption and desorption energies of the reactants are altered and therefore influence the activity of the catalyst. An electron-rich surface with good electron-donating properties is preferred for the ORR that takes place in the fuel cell cathode.

Geometric effects are divided into morphology and size [6]. Pt particles with a lower coordination number exhibit a lower activity. This difference is more prominent for smaller Pt particles due to the higher influence of the electronic effects. Support materials can also be divided into several classes with different features such as BET area, electrical conductivity, and chemical stability [7]. There are many alternatives of carbon support in fuel cell research for example graphene, carbon nanofibers, nanohorns, mesoporous carbon, and carbon black. Carbon black can be modified to different degrees of graphitization. A highly graphitized carbon black (GCB) has a layer-on-layer structure with a low and hydrophobic surface area. The low surface area and the hydrophobicity lead to a non-uniform dispersion of Pt particles. However, GCB exhibits high durability by reducing the risk of oxidation [8]. Another type of carbon support is high surface area carbon (HSAC), which is amorphous and has a high surface area. HSAC is porous and has micropores <2 nm, small mesopores 2 – 5 nm, and large mesopores 5 – 50 nm in size [9]. The Pt particles are often placed inside the micro- and mesopores. The large mesopores are used to transport gas and water to and from the Pt particles. HSAC is usually more susceptible to oxidation but instead, generates a better dispersion of Pt particles. For HSAC the Pt particles are often positioned inside the pores while for GCB, the Pt particles are placed at the edges, corners, and interface.

2.3 Degradation Mechanisms

To be able to improve the catalyst durability, knowing the mechanism behind the performance decline is essential. The degradation can be divided into primary and secondary degradation mechanisms [10]. The primary degradation generates the second degradation mechanism and could therefore cause severe performance loss on the catalyst. Pt dissolution, agglomeration, detachment and carbon corrosion are the main degradation mechanism known in fuel cells. Figure 2.2 illustrates these four degradation mechanisms.

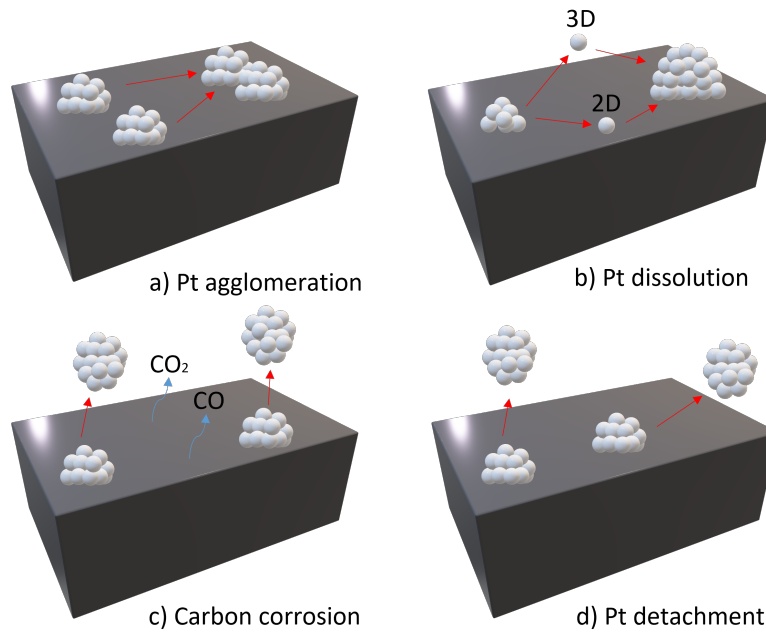
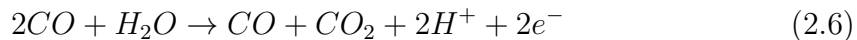
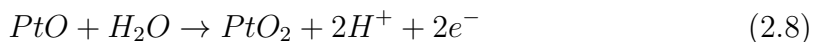
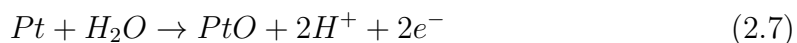


Figure 2.2: Illustrations of known common degradation mechanisms in fuel cells such as Pt agglomeration, Pt dissolution, carbon corrosion, and Pt detachment. Black box symbols are carbon support and white spheres are Pt atoms.

Carbon corrosion occurs above 1 V and the corrosion increases with increasing potential according to Reactions 2.4, 2.5, and 2.6 [6, 11]. Carbon corrosion creates a weaker Pt/C interaction. The support also exhibits structural and hydrophilic changes which in turn can result in flooding of the cathode. This causes mass transport issues because the transport of oxygen to the Pt particles is obstructed [10]. Carbon corrosion also leads to an uneven distribution of Pt particles [12]. Moreover, carbon corrosion could also be the primary degradation mechanism but initiate a secondary degradation mechanism called Pt detachment, where larger Pt particles detach from the support due to weaker Pt/C interaction. This causes a severe performance decline of the catalyst.



Pt dissolution is driven by lowering the Pt particles surface energy [12]. In Pt dissolution, Pt oxide is an important factor. The Pt oxide formation starts at ≈ 0.80 V and continues up to 1.1 V vs RHE during the anodic scan according to the Reaction 2.7. Above 1.1 V further oxidation can take place up to 1.6 V that form PtO_2 can form according to Reaction 2.8 [13, 14].



The oxidation starts with OH or O^{2-} adsorption on one or two Pt particles. The coverage will continue up to a critical level until the adatoms repulsive interactions equal the enthalpy for oxide formation. Above this critical level, it is energetically favourable for the oxygenated species to push into the Pt surface and form a sub-surface oxide layer. The formation of a sub-surface layer is referred to as the place exchange mechanism illustrated in Figure 2.3.

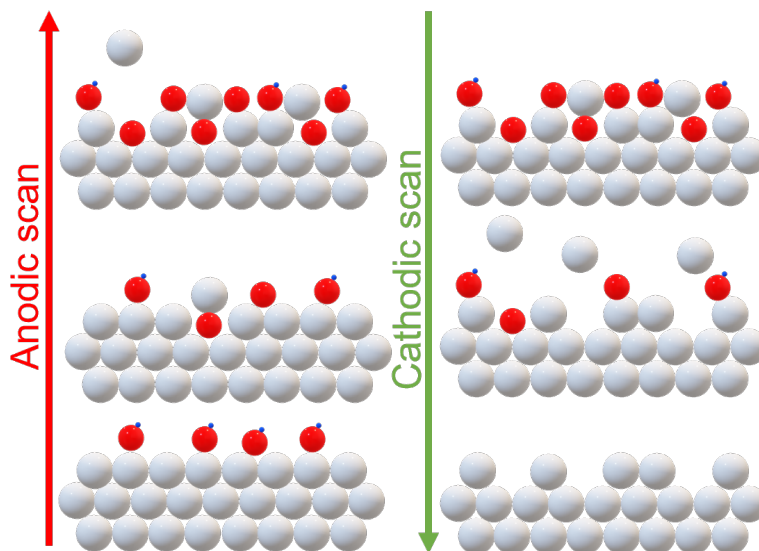


Figure 2.3: The place-exchange mechanism illustrates the Pt oxide layer formation and Pt oxide dissolution in the anodic and cathodic scans. The white, red, and blue sphere represents Pt, oxygen, and hydrogen atoms, respectively.

Topolov et. al reported in the anodic scan, only small amounts of dissolved Pt can be detected and are likely to be caused by exposed low-coordinated Pt atoms on

the surface [13]. When all the exposed sites are dissolved, the Pt dissolution ceases and the surface is fully passivated by the Pt oxide. In the cathodic scan, the Pt oxide is reduced according to Reaction 2.9. A more dominant peak of dissolved Pt is observed in the cathodic scan since there are large numbers of low-coordinated Pt atoms in the sub-surface layer. The cathodic dissolution of oxide is proposed through Reaction 2.10 and takes place in the potential interval of 0.5 – 1.1 V vs RHE [14]. The amount of dissolved Pt depends on the thickness of the Pt oxide. During the reduction, low-coordinated Pt atoms on the surface will be exposed and could dissolve.



The dissolved Pt can then be redeposited in the membrane or on bigger Pt particles. Redeposit of Pt in the membrane generates the so-called Pt band [12]. The location of this band can be correlated to the partial pressures of oxygen from the cathode and hydrogen cross-over from the anode. The exact location will be where the concentration of crossover hydrogen is high enough to reduce the dissolved Pt.

Redeposit of dissolved Pt on larger particles is called Ostwald Ripening [6]. With Ostwald Ripening, smaller particles shrink and larger particles grow and are divided into two processes, 2D and 3D. In 3D Ostwald ripening, the dissolved particles travel through the ionomer and redeposit on larger particles. In 2D Ostwald ripening, a larger and a smaller Pt particle are electrically connected to the same support. The two particles will thereby form a cell with electrons travelling through the support and the dissolved Pt will attach to the larger particle. Factors influencing Ostwald Ripening are the following. Firstly, the particle size and distribution. Pt particles with a diameter of 2 – 3 nm are more prone to dissolution while Pt particles with 4 – 5 nm diameter are much more stable. Smaller Pt particles are more prone to dissolve because of a higher solubility due to higher curvature and a higher surface energy and will therefore be more reactive at a lower potential according to the Gibbs-Thompson effect [10]. A wide Pt distribution will lead to more dissolution due to a larger surface energy difference. Secondly, a high carbon support conductivity generates an easier transfer of electrons between the larger and the smaller particles. Thirdly, high ionic conductivity of the ionomer would make it easier for the dissolved Pt to travel from the small to larger Pt particles.

Agglomeration causes particle growth [10]. This could be due to either particle migration or the collision of two particles. Factors influencing agglomeration include particle size, the shape of particles, composition, support properties, the interaction between support and catalyst, the distance between Pt particles, support pore size distribution, particles distribution on support, and operation conditions such as UPL, LPL, scan rate, temperature, and humidity [15]. A large distance between the particles is preferred to mitigate agglomeration and this can be achieved by lowering the Pt loading and tuning the support surface area and morphology [6]. Carbon corrosion could additionally lead to shrinkage of the support area and therefore

force the particles closer to each other. In addition, corrosion could also weaken the Pt/C interaction and therefore increase the agglomeration.

2.3.1 The Proximity Effect

The distance between Pt particles on the support has an effect on the catalyst activity and durability, giving rise to the so-called Proximity Effect [16, 17, 18]. The edge-to-edge distance between Pt particles on the support can be calculated by Equation 2.11. d_{ipee} is the edge-to-edge inter-particle distance, A is the total support BET area, N is the number of Pt particles, and d_{NP} is the diameter of the nanoparticles. The assumptions for the calculations are that the nanoparticles have a spherical shape, the particles are monodispersed on the surface and the Pt particles are homogeneously distributed on the support.

$$d_{ipee}(nm) = \sqrt{\frac{A(nm^2)}{N}} - d_{NP}(nm) \quad (2.11)$$

Highly dispersed Pt particles will produce a high electrochemical surface area (ECSA) enabling O_2 to be supplied to each individual Pt particle without interfering with neighbouring particles and thereby exhibiting a high ORR activity [18]. This is especially true for particles less than 3 nm in size. For Pt particles with a size of 1.8 nm, the ECSA can be increased from 80 m^2/g and reach a maximum of 130 m^2/g when the d_{ipee} increases from 1 to 5 nm.

In addition, the inter-particle distance has an effect on the catalyst degradation mechanisms agglomeration and dissolution. A high inter-particle distance lowers the probability of particle migration and agglomeration, therefore lowering the degradation rate [19]. A possible explanation for particle migration is that the Pt surface continuously changes from hydrophilic to oxophilic during the potential cycling. The carbon support is hydrophobic and the change in Pt particle properties will change how the Pt and support interact and can therefore cause migration [20]. In opposition to agglomeration, the dissolution rate will increase with a higher inter-particle distance. The increase in dissolution is proposed to be due to three mechanisms. Firstly, with decreasing inter-particle distance, the concentration of Pt ions will increase around the Pt particles. This will cause a shift in Nerst potential and decrease the anodic and cathodic dissolution. Secondly, with a smaller distance the probability increases of Pt ions re-deposition on neighbouring Pt and not diffusing into the bulk thereby decreasing the dissolution. Thirdly, with smaller distances, the Pt particles impact each other oxophilicity. Consequently, the oxidation potential is lowered which in turn decreases the dissolution.

2.4 Rotating Disk Electrode

RDE is ex-situ testing that enables a cheap, rapid, and easier analysis of the catalyst layer in fuel cells [21]. In RDE the mass transport can be controlled through diffusion and convection in a liquid electrolyte [22]. Both diffusion and convection

will determine the net transport of reactants to the surface. Diffusion is the only process when there is no rotation of the electrode. By rotating the electrode in the electrolyte, a relative motion is created that drags reactants to the electrode surface and pushes products from the electrode surface. The convection is required to measure the ORR but not for the measurement of ECSA, due to no product being produced. In real fuel cells, the reactants are transported to the catalyst as gas. Consequently, mass transport in RDE is not realistic. Additionally, there could be a difference in degradation mechanisms in RDE compared to real fuel cells. For a more realistic mass transport, in-situ testing using MEA in single, short, or full stacks can be used. However, stack testing comes with several disadvantages being costly with increasing cost in the number of cells used in the test because of higher quantities of expensive Pt catalysts. Analysis of the in-situ testing could also be complicated due to the fact that it is hard to separate and quantify which specific components in the MEA causing the degradation. Therefore, it is necessary after RDE to confirm and compare the results with stack testing.

2.4.1 Cyclic Voltammetry

Cyclic voltammetry (CV) is performed in an electrochemical cell with a working electrode, a counter electrode, and a reference electrode in an electrolyte solution. The working electrode used is the RDE and is readily used in catalyst investigations because the mass transport can be controlled. For the CV, the UPL and LPL are set and the potential is cycled between these two values in an anodic and cathodic scan. The potential is controlled between the working and reference electrode by a potentiostat, and the current is measured at the counter electrode. This produces a plot of potential vs current also referred to as a cyclic voltammogram. An example of a cyclic voltammogram for Pt in N_2 is presented in Figure 2.4.

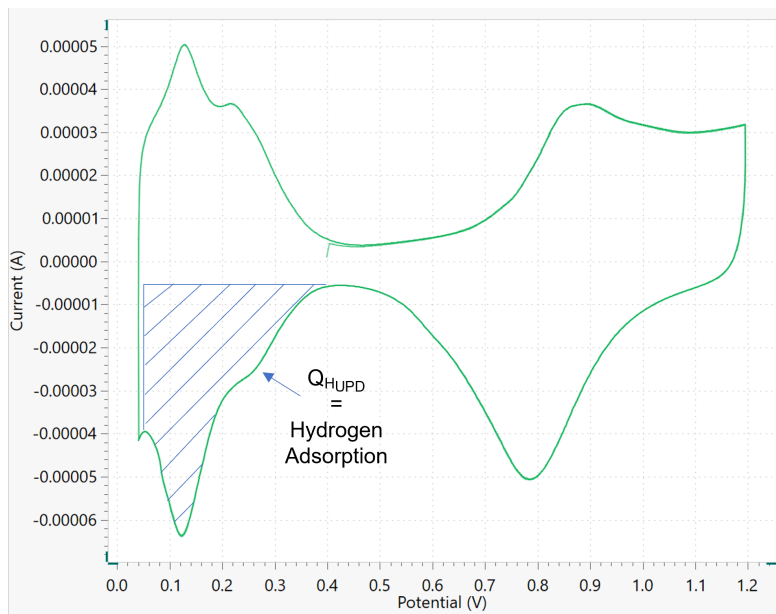


Figure 2.4: Cyclic voltammogram with current (A) vs potential (V). The blue region represents the hydrogen adsorption area is integrated to produce Q_{HUPD} .

The anodic scan occurs with an increase in potential. In the region 0.05 to 0.4 V, hydrogen desorption takes place and between 0.45 and 0.55 V the only current that flows to supply the electrolytic double layer [23]. Above 0.55 V, an increase in current is noticed that corresponds to the chemisorption of hydroxide. Above 0.8 V, the oxidation to form PtO takes place and at 1.6 V there is oxygen evolution. When the potential is reversed in direction, oxygen in the oxide layer is reduced. Between 0.4 and 0.05 V the hydrogen double layer is formed.

2.4.1.1 Electrochemical Surface Area

Electrochemical Surface Area (ECSA) is used to determine the surface area of the Pt and is presented in Equation 2.12. There are two assumptions in determining ECSA. Firstly, each Pt atom can adsorb one hydrogen atom and secondly, any charge required to complete the monolayer up to a potential of E_{min} positive to RHE, is compensated by a charge due to the hydrogen evolution current. Q_{HUPD} corresponds to the hydrogen adsorption area and is determined by integrating the potential vs current plot in the region of 0.04 – 0.4 V vs RHE. The Q_{HUPD} area is visualized in Figure 2.4. The fractional coverage of hydrogen corresponds to 0.77 and 0.210 mC/cm² is the charge of the monolayer and thereby the relationship between hydrogen adsorption/desorption. By monitoring the ECSA after a specific number of cycles, the catalyst durability can be evaluated.

$$ECSA(cm^2/g_{Pt}) = \frac{Q_{HUPD}(mC)}{0.77 * 0.210(mC/cm^2) * m_{Pt}(g)} \quad (2.12)$$

2.4.2 Accelerated Stress Tests

In fuel cells automotive it operates under four operating conditions, such as working load, high power, idling and start-stop [24]. The major contributor to fuel cell performance loss are working load and start-stop operations, although degradation may occur during all four operating conditions. Under start-stop operation, the potential difference between the anode and cathode could be as high as 1.5 V and therefore lead to severe carbon corrosion. Idling is when the fuel cell supplies energy only to the subsystems such as water pumps, superchargers, hydrogen injectors, and electrical systems. Under idling conditions, the cathode might experience potentials higher than 0.8 V and therefore accelerate agglomeration and Pt dissolution. The fuel cell experience high power under acceleration or steep hill climbing. Under these conditions, the system can experience fuel starvation, local hot spots, and water flooding of the cathode. This could in turn lead to Pt dissolution, carbon corrosion, and agglomeration. Working load corresponds to driving the automotive with varying potentials and formation of products like water and heat [5]. This causes both chemical as well as mechanical degradation of the fuel cells components. Chemical degradation could be Pt dissolution and agglomeration.

ASTs can be designed to target one operation condition or several. ASTs with RDE is a quantitative method to evaluate catalysts durability. Combining several ASTs could further complicate the analysis of the results and determine what is actually

causing the performance loss. Parameters that can be altered in the ASTs are cycle profile, electrolyte type and concentration, scan rate, hold time, and potentials interval [25]. In addition, parameters that should be presented for easier comparison between ASTs are the reference electrode used, temperature, and constants used to calculate ECSA.

Cycle profiles can be triangular and square waves either symmetrical or asymmetrical. Figure 2.5 presents different cycle profiles. Square wave exhibits a higher degradation than triangular wave [26, 27]. The enhanced degradation using square wave can be contributed to surface oxide not having enough time to form. Consequently, leaving the bare Pt surface exposed at a higher potential which results in more degradation. With a higher scan rate, it is kinetically favourable for the re-deposition of Pt ions which leads to less degradation per cycle. However, if one takes into account that many more cycles are possible with a higher scan rate the total degradation per unit of time with a higher scan rate [13]. Previously used scan rates in ASTs are in the range of 50 to 500 mV/s [11, 25, 28, 29, 30].

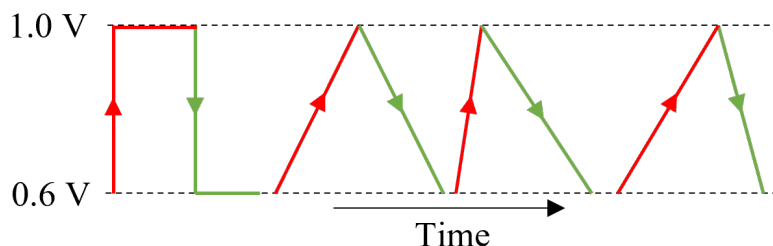


Figure 2.5: Cycle profiles square, triangular and asymmetrical triangular in the potential interval 0.6 – 1.0 V. Red is the anodic scan and green is the cathodic scan.

Electrolytes frequently used in RDE experiments are HClO_4 and H_2SO_4 . According to Topolov et.al, an increased pH generates a higher dissolution of low-coordinated Pt in both the anodic and cathodic scans. For a comparative study of catalysts, the same pH and electrolyte should be utilized. Different potential intervals are used to target different operating conditions and degradation mechanisms. Working load tests where Pt dissolution is the most prominent degradation mechanism are in the potential window of 0.6 – 1.0 V [25]. The 0.6 V is the LPL corresponding to the maximum load. 1.0 V is the UPL and the open circuit potential [27]. For start-shut down operations with high carbon corrosion, the potential window is usually set to 1.0 – 1.6 V [11, 28, 30].

3

Experimental

In this section, all the test methods, materials and instruments used in the thesis are presented.

3.1 Catalysts

Three catalysts of type Pt/C with 50 wt% Pt loadings are evaluated in this thesis. All three catalysts have different producers. Their characteristics are specified in Table 3.1. Catalysts A and B have particle size intervals of 3.4 – 4.6 nm and 3.4 – 5.1 nm, respectively. All three catalysts particle size distributions are unknown. Catalysts A and C have a carbon support of GCB with lower support areas of 80 and 220 m²/g, respectively. The carbon support for catalyst B is HSAC with a higher support area of 750 m²/g.

Table 3.1: Characteristics of catalysts investigated such as Pt size, support material, and support BET. Analysis techniques for determining particle size and carbon support area are not specified.

Catalyst	Particle Size (nm)	Support Material	Support BET (m ² /g)
A	3.4 – 4.6	GCB	80
B	3.4 – 5.1	HSAC	750
C	4	GCB	220

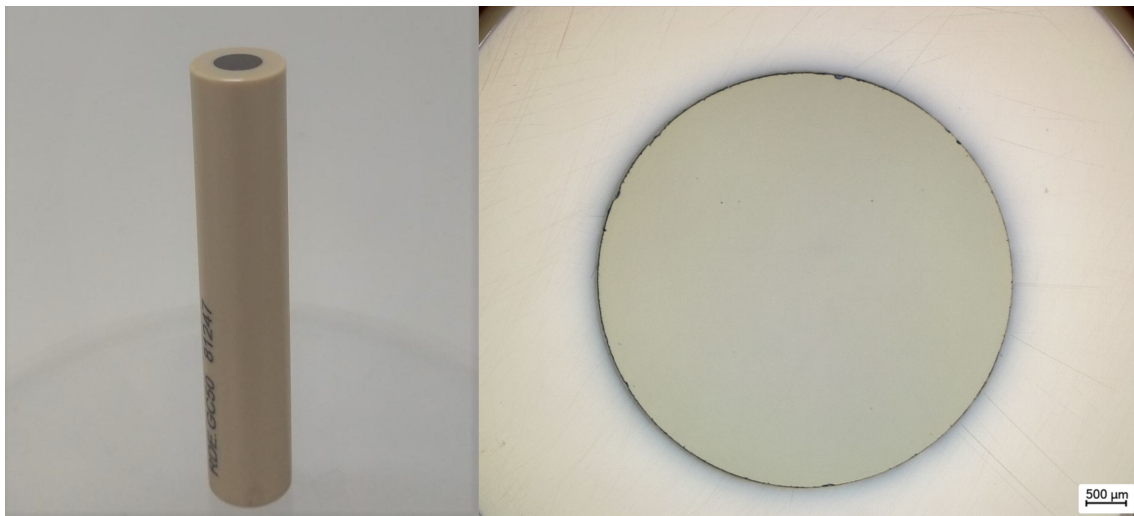
3.2 Ink Preparation

Five inks are prepared and used for ASTs. A 20 ml vial is rinsed and dried with acetone and then placed on a Sartorius microbalance. First, the catalyst is added and an anti-static gun is used to avoid static effects. Nano-pure water from Purelab Chorus 1 with a resistivity of a maximum 18.2 Mohm*cm is added to avoid spontaneous combustion. Then the ionomer Nafion™ PFSA 20 wt% Dispersion D2020, Chemours and lastly 2-propanol AnalaR NORMAPUR®Reag. Ph. Eur., Reag. USP, ACS, VWR are added. The lid of the vial is then closed to avoid evaporation of the 2-propanol. The five inks compositions are specified in Table 3.2. The overall aim for making the inks are 0.25 – 1.0 in w/w ionomer/carbon ratio, 10.0 vol% alcohol, and a Pt loading of 20.0 μg/cm².

Table 3.2: The compositions of the inks used for ASTs.

Ink	Catalyst	Ionomer/carbon	Alcohol (vol%)	Pt loading ($\mu\text{g}/\text{cm}^2$)
1	A	0.91	10.0	19.1
2	B	0.50	10.0	19.8
2	B	0.63	9.8	20.0
4	C	0.80	10.0	19.4
5	C	0.99	9.8	19.5

The inks are then dispersed using a Hielscher ultrasonic processor with a 3 mm sonotrode (S24d3). To avoid an increase in temperature during dispersion, the vial is emerged in cold water. All five inks are dispersed with 9 300 Ws energy input with an amplitude of 40%. After dispersion, the ink is left to mature for at least 2 h. After the ink maturation time, 10 μl of dispersed ink is transferred to a clean 5 mm diameter glassy carbon (GC) electrode using an automated pipette and then left to dry in air at room temperature. Figure 3.1 illustrate a clean GC electrode in polyetheretherketone (PEEK).

**Figure 3.1:** A clean GC electrode emerged in PEEK used for ASTs.

The coated electrode is then examined and photographed using a Lecia DVM6 light microscope with the settings exposure 18.5 ms, gain 1.00, RL light 50, and CXI light 60. The coating is redone if the droplet retracts/shrinks or if catalyst ink is visible outside of the GC disk. The aim is a catalyst coating that covers the whole GC disk and is not spread outside of the disk. The GC electrode was cleaned by polishing the surface with Al_2O_3 and acetone on a polishing cloth. The electrode was then rinsed with nano-pure water and acetone. When dried the clean GC electrode is checked using the microscope to confirm cleanliness.

3.3 RDE Preparation

Contamination in the RDE cell can influence the results of the test if not cleaned properly. The following cleaning procedure is performed after the cell has been in operation for 3 days. The RDE cell is soaked with 95% H_2SO_4 overnight. The other components such as the gas inlet, caps, and lid are soaked in a 10 ml/l mucosal (VWR) solution for a minimum of 30 minutes. Cells and components are then thoroughly rinsed with nano-pure water. The cell is then first washed with 0.1 M HClO_4 to remove excess water before being filled with 200 ml of electrolyte. The cell is then assembled and the electrolyte is saturated with 0.025 litres/min N_2 for a minimum of 30 minutes before any test is started. The reference electrode used is a reversible hydrogen electrode (RHE) and the counter electrode is a Pt wire. During the AST, 0.025 litres/min N_2 is directed to the surface of the electrolyte to provide an inert atmosphere. The assembled RDE is visualized in Figure 3.2.

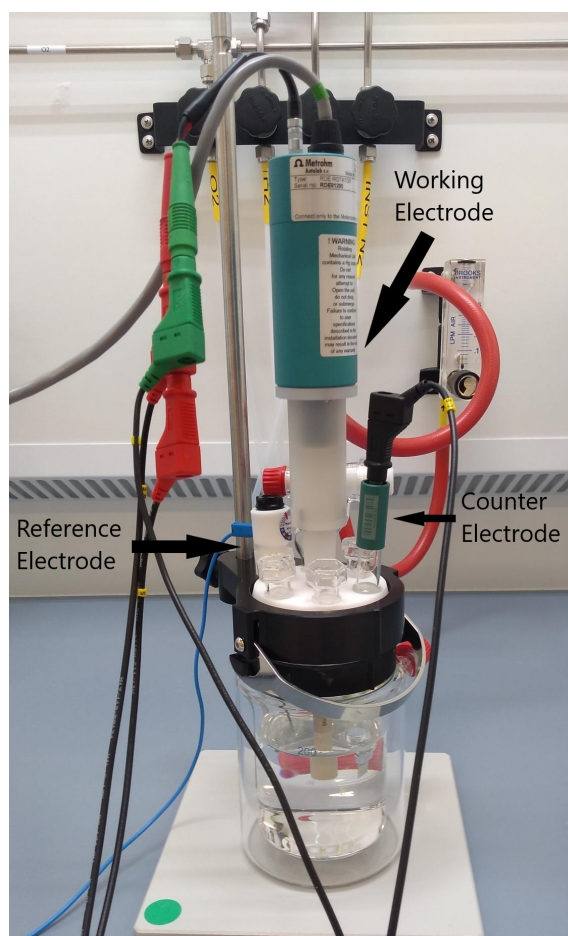


Figure 3.2: Assembled and connected RDE cell to potentiostat with reference, working, and counter electrode emerged in the electrolyte of 0.1 M HClO_4 .

3.4 Accelerated Stress Test

Five different ASTs were performed and they are presented in Table 3.3. All ASTs are performed in 0.1 M HClO₄, with a flow of 0.025 l/min N₂, and an LPL of 0.6 V. AST-1 is performed to investigate scan rate influence on the catalyst durability and the results are compared with AST-2. AST-2,3,4, and 5 investigate the UPL influence on catalyst durability using a scan rate of 50 mV/s. AST-5 adjusted investigate the conditioning and ECSA scan influence of the total degradation and is performed only with one test for catalysts A and B. AST-1, 2,3,4, and 5 are repeated three times.

Table 3.3: ASTs performed for catalyst evaluation.

AST	Scan Rate (mV/s)	UPL (V)	Catalyst
1	250	1.0	A
2	50	1.0	A,B,C
3	50	0.9	A,B,C
4	50	0.8	A,B,C
5	50	0.7	A,B,C
5 adjusted	50	0.7	A,B

Before ASTs are initiated, the coated electrodes are pre-treated with 120 conditioning scans between 0.04 and 1.2 V with a scan rate of 100 mV/s. After the pre-treatment, ECSA procedure is initiated with three scans between 0.04 and 1.2 V at 20 mV/s. From the third scan, Q_{HUPD} is integrated in the interval 0.04 and 0.4 V to calculate ECSA. The calculation of ECSA is performed using the software NOVA 2.1.5. The first ECSA of the AST is referred to as the beginning of life (BoL). After BoL, potential cycling is initiated and stopped at time 0.44, 0.89, 2.22, 3.56, 7.11, 12.44, and 17.78 h to determine the ECSA. Before each of these ECSA measurements, 20 conditioning scans in the potential of 0.04 and 1.2 V with 100 mV/s are performed and then three CV scans at 20 mV/s are performed to calculate the ECSA. Once again, the Q_{HUPD} is calculated from the third CV scan. Table 3.4 3.5, 3.6, 3.7, 3.8, and 3.9 presents the schedule for AST-1, 2, 3, 4, 5, and 5 adjusted and specify scan rate, LPL, UPL, and the number of conditioning scans for each step. The scan rate, UPL and number of cycles are different between AST 1, 2, 3, 4, and 5. However, the ECSA scans are performed at the same time interval specified above for AST-1,2,3,4, and 5. AST-5 adjusted has the same UPL and scan rate as AST-5 but the conditioning ECSA CV scans are removed to be only at BoL and 17.78 h.

Table 3.4: The schedule for AST-1. Scan rate, the number of cycles, LPL, and UPL is specified for the conditioning and procedure scans.

Procedure	Conditioning Scans		Procedure Scans			
	No.	Scan Rate (mV/s)	No.	Scan Rate (mV/s)	LPL (V)	UPL (V)
Pre-treatment, ECSA, BoL	120	100	3	20	0.04	1.2
AST, BoL – 0.44 h			500	250	0.6	1.0
ECSA	20	100	3	20	0.04	1.2
AST, 0.44 – 0.89 h			500	250	0.6	1.0
ECSA	20	100	3	20	0.04	1.2
AST, 0.89 – 2.22 h			1500	250	0.6	1.0
ECSA	20	100	3	20	0.04	1.2
AST, 2.22 – 3.56 h			1500	250	0.6	1.0
ECSA	20	100	3	20	0.04	1.2
AST, 3.56 – 7.11 h			4000	250	0.6	1.0
ECSA	20	100	3	20	0.04	1.2
AST, 7.11 – 12.44 h			6000	250	0.6	1.0
ECSA	20	100	3	20	0.04	1.2
AST, 12.44 – 17.78 h			6000	250	0.6	1.0
ECSA	20	100	3	20	0.04	1.2

Table 3.5: The schedule for AST-2. Scan rate, the number of cycles, LPL, and UPL is specified for the conditioning and procedure scans.

Procedure	Conditioning Scans		Procedure Scans			
	No.	Scan Rate (mV/s)	No.	Scan Rate (mV/s)	LPL (V)	UPL (V)
Pre-treatment, ECSA, BoL	120	100	3	20	0.04	1.2
AST, BoL – 0.44 h			100	50	0.6	1.0
ECSA	20	100	3	20	0.04	1.2
AST, 0.44 – 0.89 h			100	50	0.6	1.0
ECSA	20	100	3	20	0.04	1.2
AST, 0.89 – 2.22 h			300	50	0.6	1.0
ECSA	20	100	3	20	0.04	1.2
AST, 2.22 – 3.56 h			300	50	0.6	1.0
ECSA	20	100	3	20	0.04	1.2
AST, 3.56 – 7.11 h			800	50	0.6	1.0
ECSA	20	100	3	20	0.04	1.2
AST, 7.11 – 12.44 h			1200	50	0.6	1.0
ECSA	20	100	3	20	0.04	1.2
AST, 12.44 – 17.78 h			1200	50	0.6	1.0
ECSA	20	100	3	20	0.04	1.2

3. Experimental

Table 3.6: The schedule for AST-3. Scan rate, the number of cycles, LPL, and UPL is specified for the conditioning and procedure scans.

Procedure	Conditioning Scans		Procedure Scans			
	No.	Scan Rate (mV/s)	No.	Scan Rate (mV/s)	LPL (V)	UPL (V)
Pre-treatment, ECSA, BoL	120	100	3	20	0.04	1.2
AST, BoL – 0.44 h			133	50	0.6	0.9
ECSA	20	100	3	20	0.04	1.2
AST, 0.44 – 0.89 h			133	50	0.6	0.9
ECSA	20	100	3	20	0.04	1.2
AST, 0.89 – 2.22 h			401	50	0.6	0.9
ECSA	20	100	3	20	0.04	1.2
AST, 2.22 – 3.56 h			401	50	0.6	0.9
ECSA	20	100	3	20	0.04	1.2
AST, 3.56 – 7.11 h			1065	50	0.6	0.9
ECSA	20	100	3	20	0.04	1.2
AST, 7.11 – 12.44 h			1600	50	0.6	0.9
ECSA	20	100	3	20	0.04	1.2
AST, 12.44 – 17.78 h			1600	50	0.6	0.9
ECSA	20	100	3	20	0.04	1.2

Table 3.7: The schedule for AST-4. Scan rate, the number of cycles, LPL, and UPL is specified for the conditioning and procedure scans.

Procedure	Conditioning Scans		Procedure Scans			
	No.	Scan Rate (mV/s)	No.	Scan Rate (mV/s)	LPL (V)	UPL (V)
Pre-treatment, ECSA, BoL	120	100	3	20	0.04	1.2
AST, BoL – 0.44 h			200	50	0.6	0.8
ECSA	20	100	3	20	0.04	1.2
AST, 0.44 – 0.89 h			200	50	0.6	0.8
ECSA	20	100	3	20	0.04	1.2
AST, 0.89 – 2.22 h			600	50	0.6	0.8
ECSA	20	100	3	20	0.04	1.2
AST, 2.22 – 3.56 h			600	50	0.6	0.8
ECSA	20	100	3	20	0.04	1.2
AST, 3.56 – 7.11 h			1600	50	0.6	0.8
ECSA	20	100	3	20	0.04	1.2
AST, 7.11 – 12.44 h			2400	50	0.6	0.8
ECSA	20	100	3	20	0.04	1.2
AST, 12.44 – 17.78 h			2400	50	0.6	0.8
ECSA	20	100	3	20	0.04	1.2

Table 3.8: The schedule for AST-5. Scan rate, the number of cycles, LPL, and UPL is specified for the conditioning and procedure scans.

Procedure	Conditioning Scans		Procedure Scans			
	No.	Scan Rate (mV/s)	No.	Scan Rate (mV/s)	LPL (V)	UPL (V)
Pre-treatment, ECSA, BoL	120	100	3	20	0.04	1.2
AST, BoL – 0.44 h			400	50	0.6	0.7
ECSA	20	100	3	20	0.04	1.2
AST, 0.44 – 0.89 h			400	50	0.6	0.7
ECSA	20	100	3	20	0.04	1.2
AST, 0.89 – 2.22 h			1200	50	0.6	0.7
ECSA	20	100	3	20	0.04	1.2
AST, 2.22 – 3.56 h			1200	50	0.6	0.7
ECSA	20	100	3	20	0.04	1.2
AST, 3.56 – 7.11 h			3200	50	0.6	0.7
ECSA	20	100	3	20	0.04	1.2
AST, 7.11 – 12.44 h			4800	50	0.6	0.7
ECSA	20	100	3	20	0.04	1.2
AST, 12.44 – 17.78 h			4800	50	0.6	0.7
ECSA	20	100	3	20	0.04	1.2

Table 3.9: The schedule for AST-5 adjusted. Scan rate, the number of cycles, LPL, and UPL is specified for the conditioning and procedure scans.

Procedure	Conditioning Scans		Procedure Scans			
	No.	Scan Rate (mV/s)	No.	Scan Rate (mV/s)	LPL (V)	UPL (V)
Pre-treatment, ECSA, BoL	120	100	3	20	0.04	1.2
AST, BoL – 17.78 h			16000	50	0.6	0.7
ECSA	20	100	3	20	0.04	1.2

4

Results and Discussion

The results of the experiments are presented and discussed in this chapter. The discussion highlights the following parameters: scan rate, UPL, and support material influence on the catalyst degradation. In addition, possible causes for variations in test results and possible improvements are discussed.

4.1 Scan Rate

In AST-1 and AST-2, the effect of scan rates of 50 and 250 mV/s on catalyst durability is investigated. An analysis of the results is presented in Figure 4.1. There is a difference between the results after 1 h where the scan rate of 250 mV/s exhibits a greater loss of ECSA than the scan rate of 50 mV/s. The result is a higher ECSA loss of 26% for 250 mV/s compared to 23% for 50 mV/s.

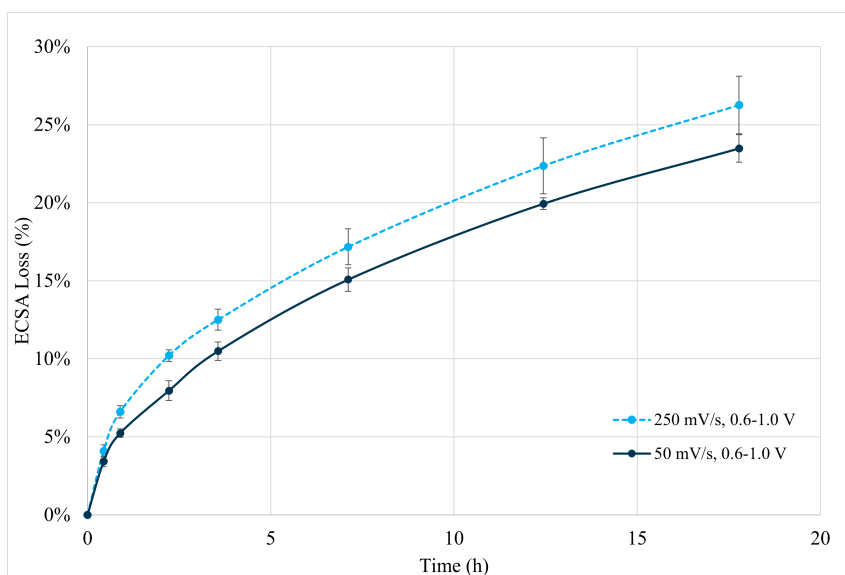


Figure 4.1: Average degradation for Catalyst A with an UPL 1.0 V for scan rate 250 (light blue) and 50 (dark blue) mV/s up to 17.78 h of potential cycling. The standard deviation and average is calculated from three repetitions.

Small particles have higher surface energy, making them more prone to dissolve, resulting in higher initial ECSA losses. Topolov et.al and Uchimura et.al both concluded that a higher scan rate results in higher degradation per unit of time [31, 26]. A higher scan rate favours the re-deposition of Pt ions and will lead to less degradation per cycle. However, if you take into account that there are 5x more cycles performed for 250 mV/s compared to 50 mV/s during the same time period. Therefore, it will be a higher total degradation with a higher scan rate. This is in agreement with the results presented in Figure 4.1.

An initial test was conducted for each scan rate of 50 and 250 mV/s to determine the influence of the scan rate on degradation. The initial results indicated that there was no difference between the two scan rates. Consequently, the decision was made to continue investigating the influence of UPL on catalyst degradation at 50 mV/s. PowerCell fuel cells operate at a scan rate up to 50 mV/s, which was the reason behind designing the ASTs with that scan rate. Afterwards, two additional tests with 50 mV/s were conducted. Three months after the initial test, tests 2 and 3 were repeated at a scan rate of 250 mV/S. Accordingly, the total ECSA losses for tests 1, 2, and 3 with a scan rate of 250 mV/s are 24.2%, 28.6%, and 26.0%, respectively. These results could be caused by the expected deviations and uncertainties of the tests. Another plausible explanation is that the ink age may affect the degradation of the catalyst. In order to verify the results in Figure 4.1, three tests should be repeated with a new ink within a shorter time frame at a scan rate of 250 mV/s to eliminate the possibility of ink ageing influencing the results.

4.2 Upper Potential Limit

The following section presents the results of ASTs- 2,3,4, and 5 for catalysts A, B, and C. Accordingly, ASTs- 2,3,4, and 5 refer to UPLs of 1.0, 0.9, 0.8, and 0.7 V, respectively. During all experiments, the LPL was 0.6 V and the scan rate was 50 mV/s.

4.2.1 Catalyst A

Figure 4.2 presents the absolute ECSA for catalyst A ink 1 with UPL 1.0, 0.9, 0.8, and 0.7 V. Average ECSA at BoL is 51.5 m²/g and ECSA at time 17.78 h is in the interval 37 – 42 m²/g. ECSA loss rates are highest for all 12 tests in the region, BoL to 2 h. In the region 2 to 17.78 h the ECSA appears to be declining at the same rate. "0.8 V, Experiment 4_ink1" and "0.8 V, Experiment 7_ink1" both demonstrate a significantly higher ECSA at BoL than the other ten experiments. A plausible reason for higher ECSA at BoL is that the vial has not been shaken to a homogeneous solution before GC electrode coating. As a result, there may be an increase in the catalyst loading, resulting in an increase in the total mass of Pt on the electrode disk.

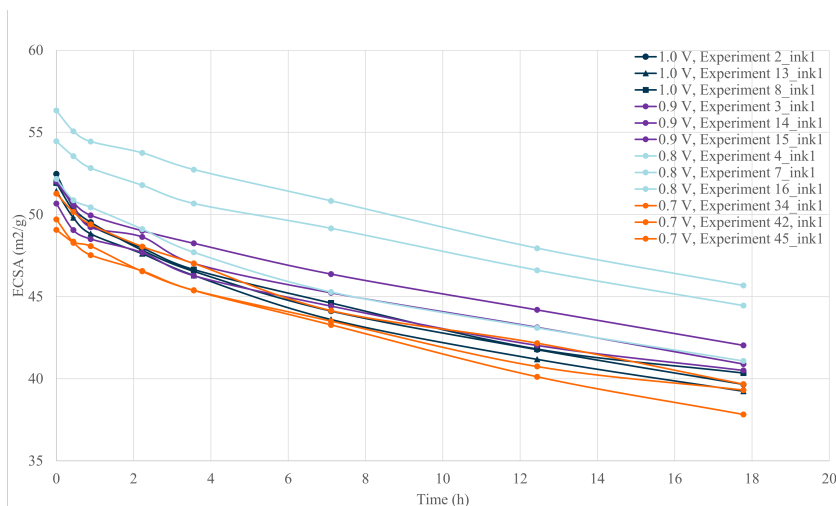


Figure 4.2: ECSA (m^2/g) over time (h) for Catalyst A, ink 1 at UPL 1.0 (dark blue), 0.9 (purple), 0.8 (light blue), and 0.7 (orange) V up to 17.78 h with a scan rate of 50 mV/s. Each UPLs has three repetitions.

ECSA loss over time for catalyst A ink 1 with UPL 1.0, 0.9, 0.8, and 0.7 V is presented in Figure 4.3. There is a higher ECSA loss rate up to 2 h before it decreases and the total ECSA loss at 17.78 h for each UPL is 23.4, 21.2, 19.5, and 22.1%, respectively. There is a higher degradation of UPL 0.7 compared to UPL 0.8 and 0.9 V. This could be due to the ageing of the ink. Testing of UPL 1.0, 0.9, and 0.8 was conducted three months prior to testing at UPL 0.7 V. The low total ECSA loss of 19.5% at UPL 0.8 V could be affected by the higher ECSA at BoL for experiments "0.8 V, Experiment 4_ink1" and "0.8 V, Experiment 7_ink 1" as visualized in Figure 4.2.

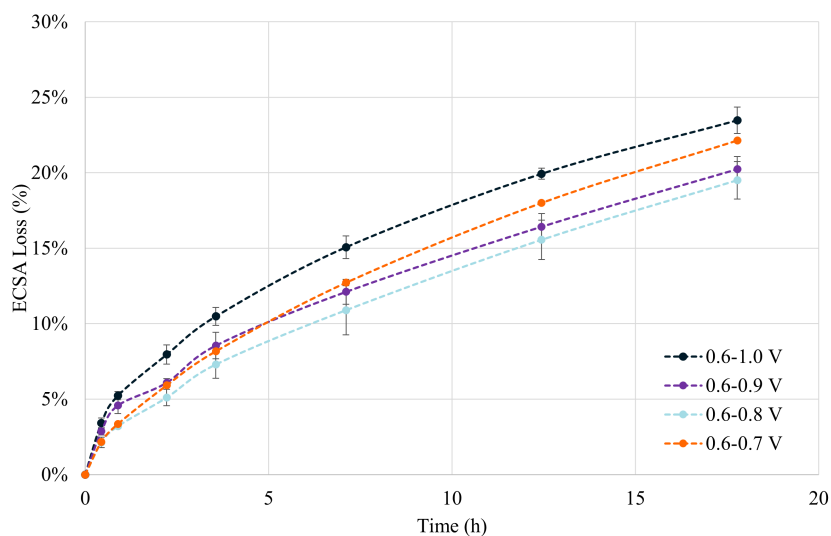


Figure 4.3: Average ECSA loss (%) over time (h) for Catalyst A, ink 1 at UPLs 1.0 (dark blue), 0.9 (purple), 0.8 (light blue), and 0.7 (orange) V up to 17.78 h a scan rate of 50 mV/s. The average and standard deviation is based on three repetitions.

4.2.2 Catalyst B

A study of the UPL effect on catalyst B degradation was conducted using inks 2 and 3. The results are presented in Figure 4.4. There is a $10 \text{ m}^2/\text{g}$ difference in ECSA at BoL between ink 2 and 3. Ink 2 has an ECSA at BoL is $\sim 107 \text{ m}^2/\text{g}$ and for ink 3 the ECSA is $\sim 95 \text{ m}^2/\text{g}$. In Section 4.4.1, the differences between the two inks are discussed in more detail. Similar to catalyst A, ECSA rapidly declines from BoL to 2 h and then slower from 2 h to 17.78 h. Test "1.0 V, Experiment 9_ink 2" has an ECSA of $115 \text{ m}^2/\text{g}$ at BoL which is considerably higher than the other results from ink 2.

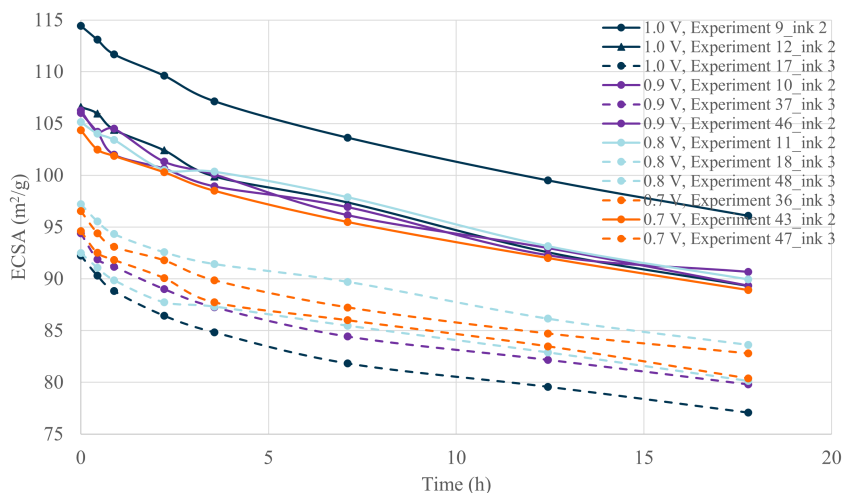


Figure 4.4: ECSA (m^2/g) over time (h) for Catalyst B, ink 2 (solid line) and 3 (dashed line) at UPLs 1.0 (dark blue), 0.9 (purple), 0.8 (light blue), 0.7 (orange) V up to 17.78 h with a scan rate of 50 mV/s . Each UPLs has three repetitions.

Both ink 2 and 3 were used in the investigation of the UPL effect on catalyst durability. Figure 4.5 illustrates the average degradation for UPL 1.0, 0.9, 0.8 and 0.7 V. The total ECSA for each UPL is 16.2, 15.3, 13.9, and 14.7%, respectively.

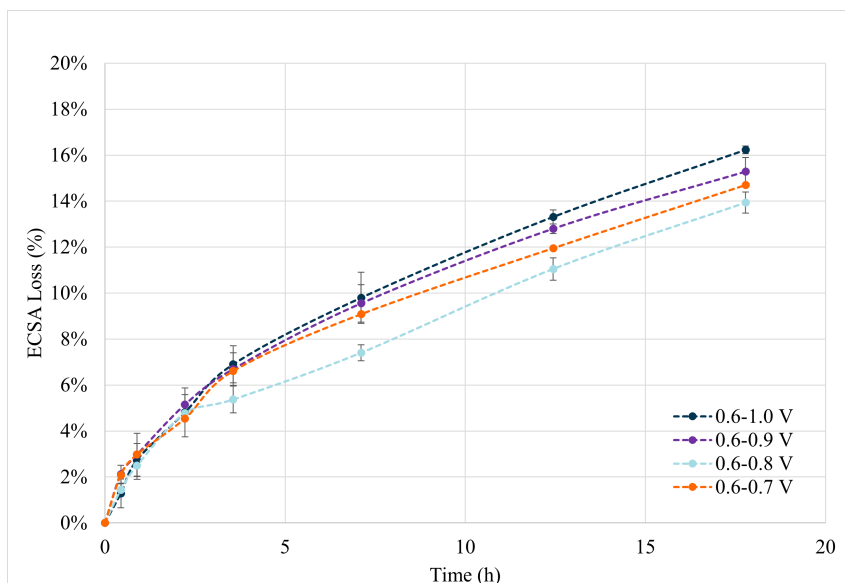


Figure 4.5: ECSA loss (%) over time (h) for Catalyst B, ink 2 (solid line) and 3 (dashed line) at UPLs 1.0 (dark blue), 0.9 (purple), 0.8 (light blue), and 0.7 (orange) V up to 17.78 h with a scan rate of 50 mV/s. The average and standard deviation is based on three repetitions.

4.2.3 Catalyst C

Figure 4.6 illustrates the effects of UPL on catalyst C with ink 4 and 5. At BoL, inks 4 and 5 have an ECSA of approximately 73 and 70 m^2/g , respectively. ECSA loss rates are highest between BoL and 2 h, and then decrease.

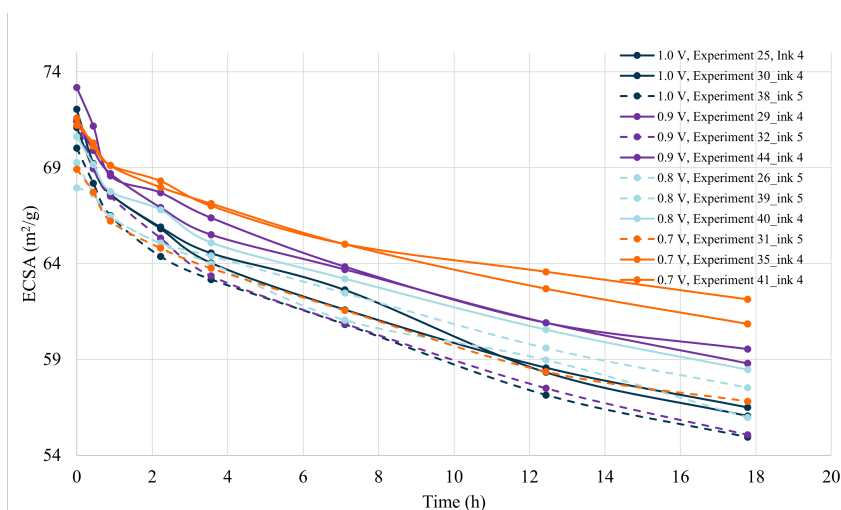


Figure 4.6: ECSA (m^2/g) over time (h) for Catalyst C, ink 4 (solid line) and 5 (dashed line) at UPLs 1.0 (dark blue), 0.9 (purple), 0.8 (light blue), 0.7 (orange) V up to 17.78 h with a scan rate of 50 mV/s. Each UPLs has three repetitions.

The average ECSA loss for Catalyst C is presented in Figure 4.7. Total ECSA loss for UPL 1.0, 0.9, 0.8 and 0.7 V is 21.4, 19.8, 17.3, and 15.1%, respectively. All test

were performed within a month. All UPL have a rapid degradation from BoL to 2 h, but UPLs 1.0 and 0.9 continue to degrade more rapidly than UPLs 0.8 and 0.7. This is likely due to a minimum oxide formation at UPL 0.8 and 0.7 V, which results in lower dissolution of low-coordinated Pt atoms.

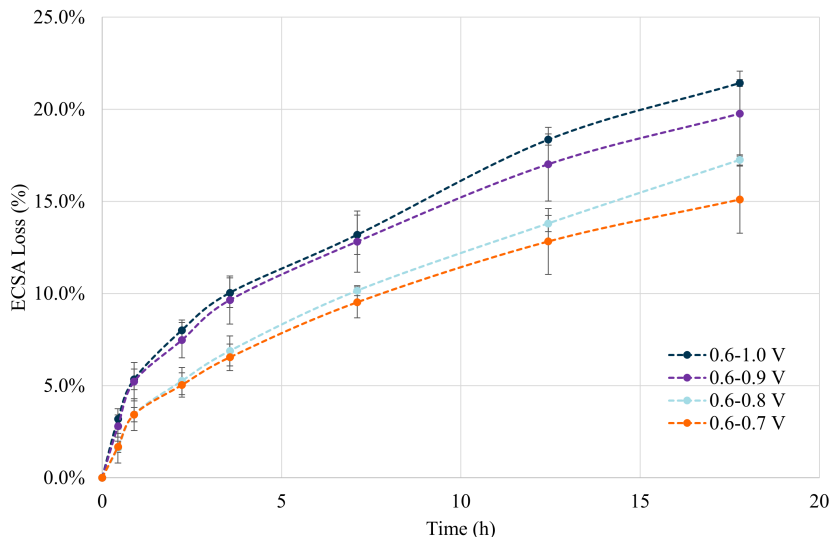


Figure 4.7: ECSA loss (%) over time (h) for Catalyst C, ink 4 and 5 at UPLs 1.0 (dark blue), 0.9 (purple), 0.8 (light blue), 0.7 (orange) V up to 17.78 h with a scan rate of 50 mV/s. The average and standard deviation is based on three repetitions. The average and standard deviation is based on three repetitions.

4.2.4 Comparison of Catalyst A, B, and C

In order to increase the durability of the catalyst, it may be necessary to limit the UPL. Figure 4.8 presents the total ECSA loss at UPLs 1.0, 0.9, 0.8, and 0.7 V for catalysts A, B, and C. The loss of performance is highest for catalyst A at all UPLs, while the loss of performance is lowest for catalyst B. Catalyst A exhibits a decline in ECSA loss at UPLs 1.0, 0.9, and 0.8 from 23 to 20%. Pt oxide begins to form between 0.8 and 0.9 V, and with increasing potential, a thicker layer of Pt oxide forms [13]. As a result of a thicker layer, a greater number of low-coordinated atoms are able to dissolve. There is no oxide formation below 0.8 V, so the ECSA loss cannot be attributed to Pt oxide dissolution.

There was an increase in total degradation for catalysts A and B, while there was a decrease in ECSA loss for catalyst C at UPL of 0.7 V. Xing et. al has presented results which examine how much dissolved Pt can be detected during cycling in the potential window 0.6 – 0.7 V [14]. The results presented are that there is no or negligible dissolution in the potential window of 0.6 – 0.7 V. This confirms the theory presented by Topolov et. al that the Pt dissolution occurs mainly in the oxidation and reduction of Pt oxide [13]. At a UPL of 0.7 V, there is no or little oxide formation and therefore no dissolution of Pt occurs. Potential cycling also induces migration and agglomeration due to changes on the Pt surface [20]. Agglomeration

can be the reason for ECSA loss at a UPL of 0.7 V. However, the increase seen in catalysts A and B can not be explained by these two theories. Analysis methods using TEM and ICP-MS could disclose what type of degradation mechanism causes the ECSA loss. Error sources such as ink age could also possibly cause the higher ECSA loss for 0.7 to 0.8 V. To confirm the results for catalysts A and B and exclude influence from ink age and other error sources, it is recommended that the tests be repeated in the potential window of 0.6 to 0.7 V. Old ink comes with several error sources such as contamination, evaporation of the solvent, and non-homogeneous solution. Traces of possible contamination could also be observed in Figure A.1 in Appendix A. According to previous in-house experiments conducted by PowerCell, ink age contributes somewhat to the deviations in ECSA testing. Nevertheless, little is known about how the ink age influences the degradation of the catalyst and further research is necessary.

The lowest total ECSA loss is observed at all UPLs for catalyst B. ECSA loss declines from 16 – 14% at UPLs 1.0, 0.9, and 0.8 V and increases by 0.5% at UPL 0.7 V. The difference between UPL 0.8 and 0.7 V is within the error bars and therefore no significant difference can be observed. Consequently, catalyst B would benefit least from voltage clipping at UPLs of 0.7 to 1.0 V. The difference in ECSA loss between UPL 0.8 and 1.0 V for catalysts A and C is the greatest, and voltage clipping would increase its durability.

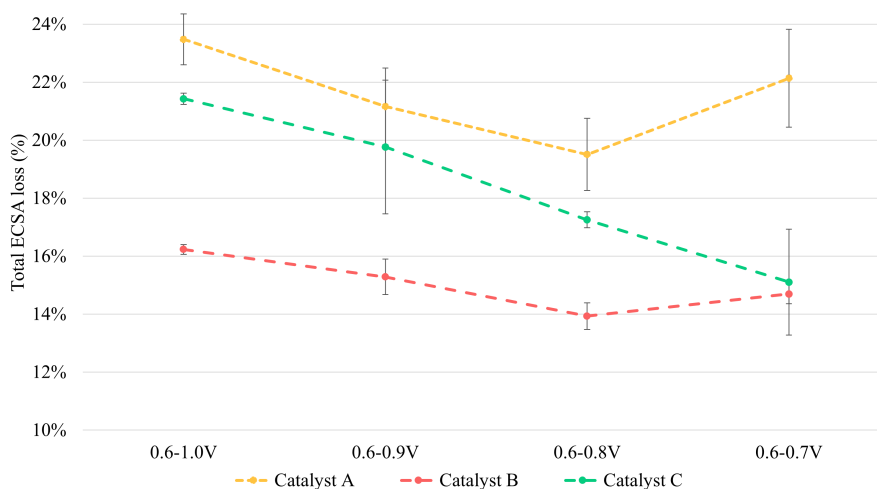


Figure 4.8: Average total ECSA loss (%) of Catalyst A (yellow), B (red) and C (green) at UPLs 1.0, 0.9, 0.8, 0.7 V at 17.78 h with a scan rate of 50 mV/s. The average and standard deviation are from 3 repeated tests for each potential limit.

The percentage loss of ECSA is a function of the ECSA at BoL, which for catalysts A, B, and C is 51, 102, and 70 m^2/g , respectively. Figure 4.9 presents the absolute value of the ECSA loss at 17.78 h. Compared to the percentage loss, the results are inverted, with catalyst B having the highest absolute ECSA loss of 17 – 14.5 m^2/g followed by catalyst C and A with 15 – 10.5 and 12 – 10.5 m^2/g , respectively. Moreover, catalyst A which has an increase in percentage loss between UPL 0.8 and

4. Results and Discussion

0.7 V seems to have an increase of $0.5 \text{ m}^2/\text{g}$, which is within the standard deviation.

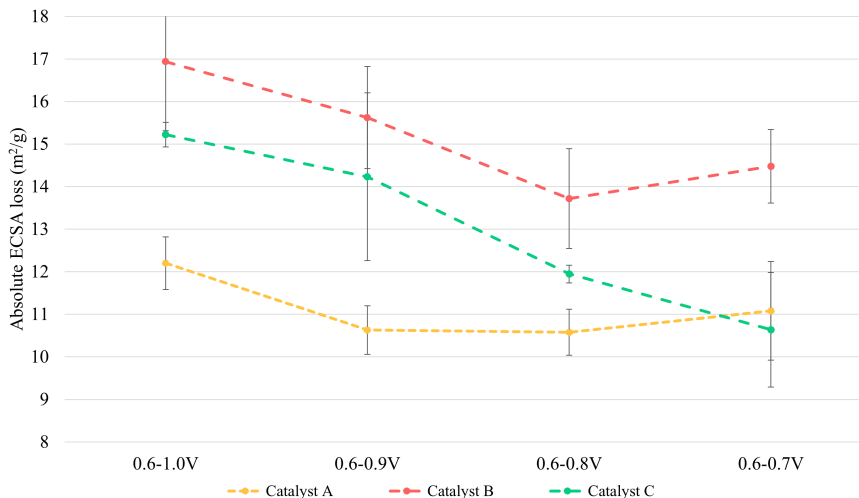


Figure 4.9: Average absolute total ECSA loss (m^2/g) for Catalyst A (yellow), B (red) and C (green) at UPL of 1.0, 0.9, 0.8, 0.7 V at 17.78 h with a scan rate of 50 mV/s. The average and standard deviation are from three repeated tests for each potential limit.

It is evident from the results presented in this section that a lower UPL will decrease the ECSA loss for all catalysts. As a result, Catalyst A appears to have the highest degradation rate, followed by Catalyst C and Catalyst B. Ideally, the catalyst should exhibit high activity and durability. Therefore, catalyst B which has both the highest activity and durability is superior to catalysts A and C.

4.3 Support Material

Catalyst durability is affected in a number of ways by the support, one important parameter is the support BET area. Catalysts A, B, and C have support BET areas of 80, 750, and 220 (m^2/g), respectively. Figure 4.10 illustrates the ECSA loss at UPL 1.0, 0.9, 0.8, and 0.7 V in relation to support BET area. According to the results, a large BET area will cause lower ECSA losses compared to a catalyst with a low support BET area.

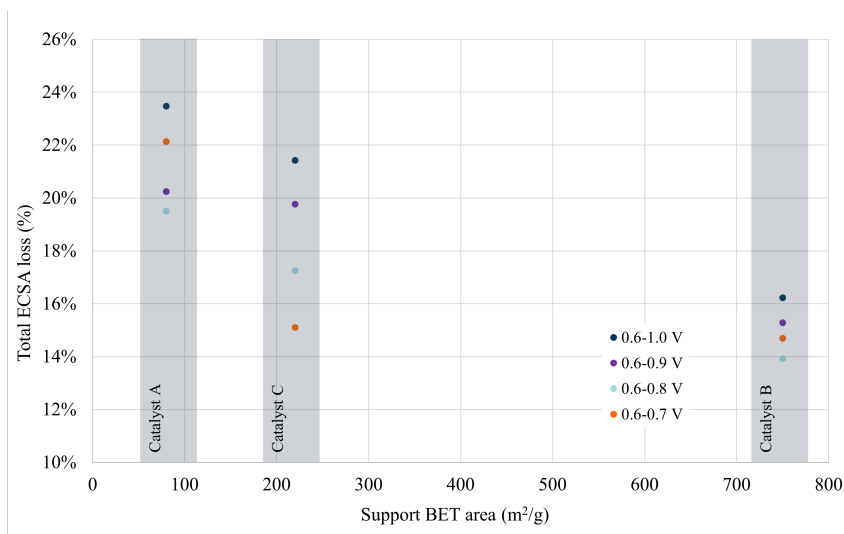


Figure 4.10: Average total degradation in (%) for catalysts A, B, and C at UPLs of 1.0 (dark blue), 0.9 (purple), 0.8 (light blue), and 0.7 (orange) V at 17.78 h with a scan rate of 50 mV/s.

In catalysts with high support BET area, ECSA loss may be lower due to an increase in the distance between particles. The inter-particle distance is calculated from the Equation 2.11. Catalysts A, B, and C have inter-particle distances of 3.8, 20.8 and 9.5 nm, respectively. In Table 4.1, the variables and inter-particle distances are presented. The Pt loading is approximately 50% and the mean Pt size is approximately 4 nm for all three catalysts. Consequently, a higher BET area results in a greater distance between particles. As a result of the proximity effect, the distance affects the activity and durability of the catalyst. Increasing the inter-particle distance increases the activity and reduces degradation caused by agglomeration, however, it increases the rate of dissolution [17]. Thus, the total degradation is governed by two competing processes. The supports morphology could also affect the agglomeration. Moreover, the Pt particle size distributions, which are unknown, have an important influence on the dissolution process. As a result of different surface energies between the particles, a wider distribution would result in a greater degree of dissolution. To determine which factor has the greatest effect on dissolution, it would be of great interest to determine the Pt size distribution for all catalysts.

Table 4.1: The inter-particle distance $I_{p_{ee}}$ has been calculated for catalysts A, B, and C according to Equation 2.11 with the parameters Pt loading (wt%), particle size (nm), and BET area (m^2/g) retrieved from the supplier.

Catalyst	Loading (wt%)	Pt size (nm)	BET (m^2/g)	$I_{p_{ee}}$ (nm)
A	0.488	4	80	3.8
B	0.5	4.3	750	20.8
C	0.465	4	220	9.5

4.4 Accuracy of Method

The accuracy and repeatability of the results are essential for all professional research. The literature on catalyst inks and coatings does not provide consistency in terms of how they are prepared and how the preparation method impacts the results. The ECSA measurements are more stable than other tests, such as the ORR test, which provides information such as the mass activity and specific activity of the catalyst. Nevertheless, it is important to critically evaluate the method used for preparing inks and coatings for RDE testing.

4.4.1 ECSA variations

For all completed tests, the ECSAs at BoL are presented in Table 4.2. An estimation of the average and the deviation is made for each individual ink as well as a combination of inks. With the exception of catalyst "B, ink 2,3", all ink combinations have a deviation of less than 4%. The catalyst "B, ink 2,3" has a deviation of 6.7%, owing to a large variance in average ECSA between inks 2 and 3, i.e. 107.2 and 94.6 m^2/g , respectively. A number of factors may be responsible for this, including weighing error, differences in dispersion time, non-homogeneous solution, and coating quality. It is possible that the balance may have been affected by a ventilation issue in the lab during the production of inks 2 and 3. A weight error of ± 0.1 mg results in an increase or decrease of 3 m^2/g . Despite this, the results of inks 2 and 3 were included in the investigation of the UPL effect on catalyst degradation since the degradation appears to be the same for both inks. Dispersion of inks 2 and 3 was carried out at 40% amplitude and 9 300 Ws of energy for both inks. It should be noted, however, that the height at which the sonotrode is positioned in the solution varies, and this results in a variation in the dispersion time. The dispersion time was 51 and 53 minutes for inks 2 and 3, respectively. To which extent dispersion time influences the ECSA requires further investigation. Before coating, the ink should be allowed to mature for at least 2 h. The inks are stored and reused for up to 3 months. During maturation and storage, larger particles that are not dispersed settled to the bottom. To ensure a homogeneous solution, the ink is shaken prior to each coating. It is however not possible to determine whether a solution is homogeneous in an exact manner.

Table 4.2: Average and standard deviation ECSA (m^2/g) at BoL. The number of experiments for the determination of average and standard deviation is denoted as n.

Catalyst	Ink	Average (m^2/g)	Std Dev (%)	n
A	1	51.5	3.5	17
B	2,3	101.4	6.7	13
B	2	107.2	3.1	7
B	3	94.6	2.0	6
C	4,5	70.4	1.8	18
C	4	71.1	1.3	11
C	5	69.5	1.6	7

Using a pipette, $10 \mu\text{l}$ of ink is placed on the GC. The droplet is stationary air dried. A smooth and uniform coating covering the entire GC electrode is the objective. Figure 4.11 shows a few examples of microscope images of the coated samples, to illustrate the difference in coating quality.

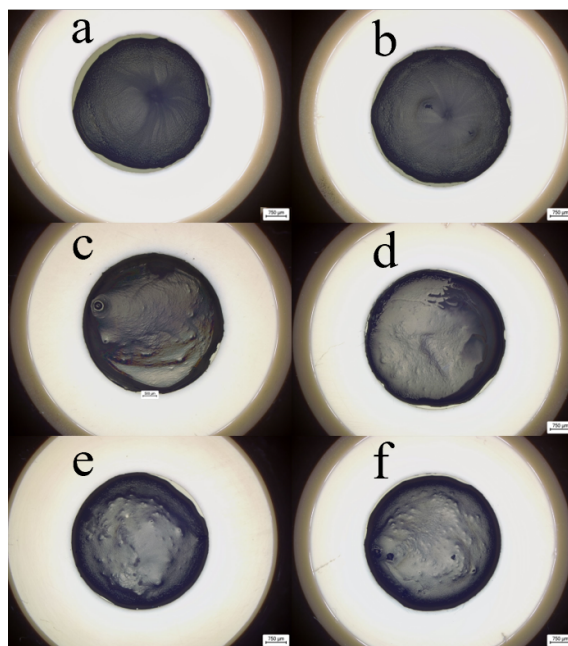


Figure 4.11: Microscope images of six coatings that are used for ASTs. a) ink 1 with Catalyst A, b) ink 1, Catalyst A, c) ink 2, catalyst B, d) ink 3, catalyst B, e) ink 4, catalyst C, f) ink 5, catalyst C.

As can be seen from the images, the objective of producing a uniform and smooth coating has not been achieved. There are dark and bright spots in the coating that indicate thicker and thinner areas, respectively. In all six specimens, there is a visible coffee ring at the edge of the GC. The coffee rings in specimens a and b are less prominent. In specimens c, e, d, and f, there are clear dots in the coating, which are catalyst agglomerates. Garsany et. al investigates the importance of coating quality

[32]. According to Garsany et. al bad, intermediate, and good coating quality tested in 0.1 M HClO_4 , 30 °C, resulted in ECSA of 42, 57, and 61 m^2/g , respectively. Bad coating quality generates a lower current over a full potential window. According to Garsany et. al both ink formulation and drying condition of the ink affects the coating quality. The use of dispersion with a higher amplitude or a higher energy input may help to reduce the agglomerates in coatings. It may also be possible to improve the coating by using a spin-dryer under the flow of N_2 instead of letting it dry by air. Spin-drying could mitigate the coffee ring and further improve the smoothness of the coating.

4.4.2 Conditioning Scans

In order to determine how much the conditioning and ECSA CV scans affect the total ECSA loss, AST-5 was adjusted. The adjusted AST-5 contained only conditioning and ECSA CV scans at BoL and 17.78 h and was performed on catalysts A and B. Figure 4.12 illustrate the results of AST-5 with catalyst A and B in potential window 0.6 – 0.7 V, and the results of the adjusted AST-5 with conditioning and ECSA CV scans only at BoL and 17.78 h. For catalyst A, the potential window 0.6 – 0.7 V results in a total ECSA loss of 22.1% and adjusted AST-5, 16.4%. The loss of catalyst B in the same tests was 14.7 and 10.9%, respectively. To provide a general guideline, the true ECSA loss to the potential cycling is 75% of the total ECSA loss for all potential windows and catalysts. For reliable results of the amount of ECSA loss that can be attributed to conditioning and ECSA CV scans, it is necessary to repeat the experiments for all possible windows and catalysts. The probable outcome is that with a higher UPL, the influence of the conditioning and ECSA CV scans will reduce.

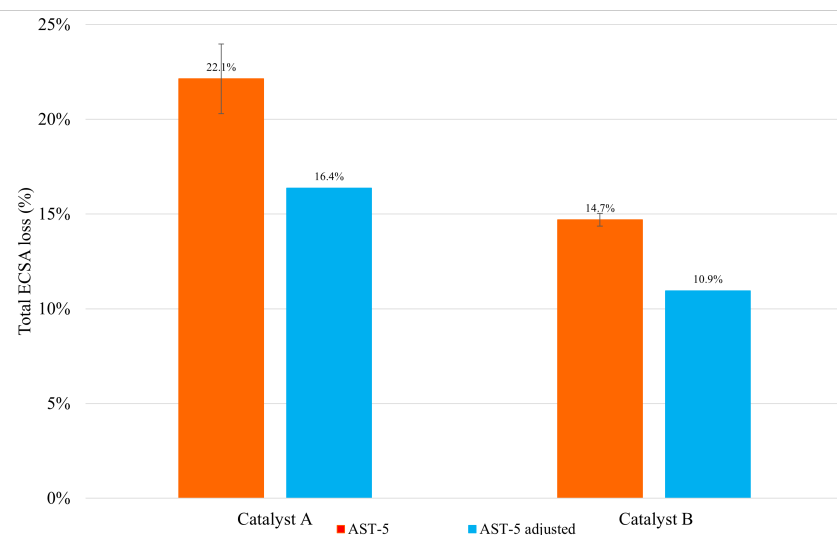


Figure 4.12: Total ECSA loss (%) of catalyst A and B for AST-5 in the potential window 0.6 – 0.7 V (orange) and for adjusted AST-5 with conditioning and ECSA scans at BoL and 17.78 h (blue). The error bars show the standard deviation, based on three repetitions.

5

Conclusions

This thesis examines the influence of scan rate, UPL, and support influence on the catalyst degradation with RDE. Furthermore, the causes and pathways for Pt degradation have been identified from the available literature. Catalyst A was tested at 50 mV/s and 250 mV/s scan rates. According to the results, ECSA loss decreased from 26 to 24% with a slower scan rate from 250 mV/s to 50 mV/s, respectively. At a scan rate of 50 mV/s, the lower degradation is attributed to the favoured re-deposition of already dissolved Pt ions.

The ASTs for catalysts A, B and C were performed with UPLs of 1.0, 0.9, 0.8, and 0.7 V. The results show a decrease in ECSA loss with decreasing UPLs of 1.0, 0.9, and 0.8 V. This could be attributed to a thinner Pt oxide layer, and a reduced number of low-coordinated Pt atoms at lower UPLs. The two main degradation mechanisms during load cycling are Pt dissolution through Ostwald Ripening and agglomeration. Catalyst A with a support BET area of 80 m²/g has the highest degradation of 23, 21, and 19% at UPLs 1.0, 0.9, and 0.8V. Catalyst B, on the other hand, with the highest support BET area of 750 m²/g exhibited the least degradation of 16, 15, and 14% at UPLs 1.0, 0.9, and 0.8 V. A higher support BET area gives a longer inter-particle distance if the Pt particles are evenly distributed on the support, which in turn reduces the degradation caused by agglomeration. Moreover, the support morphology influences agglomeration. For example, catalyst B with a HSAC, has Pt particles inside the pores which could act as a geometric barrier for Pt migration and agglomeration. Catalysts A and C using GCB have instead a more smooth surface that does not hinder Pt particle migration and agglomeration. In conclusion, a high support BET area and a morphology with many pores reduce the catalyst degradation by agglomeration, which in turn would explain the lower degradation seen for catalyst B.

Decreasing the UPL from 0.8 to 0.7 V resulted in a lower ECSA loss for catalyst C, but not for catalysts A and B. In fact, for catalysts A and B the ECSA loss was higher with a the lower UPL of 0.7 V. However, for catalyst B the increase falls within the standard deviation for UPL 0.8 and 0.7 V. The increase for catalyst A is possibly caused by the ageing of the catalyst ink or an artefact of how and how many CV scans were performed during the AST. It is estimated that 25% of the total degradation in each AST is due to the conditioning and ECSA scans, while the remaining 75% is due to the potential cycling between 0.6 – 0.7 V. Due to its greater difference in ECSA loss between UPL 1.0 and 0.8 V, catalyst A is likely to benefit most from voltage clipping. Voltage clipping should be placed at a potential

where Pt oxide formation is minimal or nonexistent, in order to reduce the amount of low-coordinated Pt atoms available for dissolution. Voltage clipping should, however, be implemented only after further improvements have been made to the RDE method and single cell tests have been performed.

5.1 Outlook

Based on the results presented in this thesis, it is evident that ink preparation and coating are not well controlled, especially for catalyst B. To minimize deviations, efforts should be made to understand how and at what parameters the spin-dryer can be used to produce smoother and more uniform coatings. PowerCell should conduct a more comprehensive study with all catalysts in-house to determine the exact parameters for the dispersion of ink. In order to produce a uniform and smooth coating, different catalysts require different parameters. Therefore, an established ink recipe for each catalyst would reduce ink production time and give a better controlled method. It is also necessary to improve coating quality in order to be able to measure the ORR that is of interest to investigate in order to understand how voltage clipping should be implemented.

The design of the ASTs used in this thesis should be evaluated and altered to provide a more accurate image of how much of the degradation is caused by the potential cycling and how much is caused by conditioning before the ECSA measurements. The potential cycling in AST 1 to 5 does not exceed 1.0 V, however, the conditioning and CV scans are in total 23 scans and set to a UPL of 1.2 V. Therefore, the recommendation is to reduce the conditioning scans and CV scans to 1.0 V to minimise degradation at higher potentials. In addition, the number of conditioning scans can be reduced. After reviewing the cyclic voltammograms, the first out of the scan have a larger shape difference than the remaining scans. Therefore, the number of scans can be reduced from 23 to only 3 scans.

There is a lack of information regarding particle size and particle size distribution before and after ASTs. The determination of these parameters would facilitate a more accurate conclusion regarding which parameters influence catalyst degradation within the potential window of 0.6 – 1.0 V. These parameters may be determined for example by TEM. Furthermore, TEM can provide information about the distribution of Pt particles on the support, allowing one to determine a more accurate inter-particle distance.

This thesis examines the durability of catalysts using RDE. The RDE differs from in-situ, which is performed in real operating conditions with realistic mass transport. The cost of stack testing will increase as the number of cells increases. In addition, other components in stack testing will influence, deteriorate and complicate the analysis, but the results will still better mimic real operating conditions than those obtained by RDE. ASTs were performed for 17.78 h. Consequently, it is unknown how the catalyst will continue to degrade after this point. Either the

catalyst will continue to degrade at the same rate as at 17.78 h or it will reach a plateau where no or little degradation is evident. It is therefore recommended that ASTs be performed for a longer period of time. Nevertheless, the 17.78 h of AST performed in this thesis is substantially shorter than the total expected lifetime of a fuel cell.

In order to integrate fuel cells into society as energy converters, catalyst utilization must be optimized and improved. Therefore, voltage clipping represents an important step toward improving the system. The purpose of this thesis is to quantitatively examine the effects of UPL on catalyst degradation during load cycling. It would be beneficial to focus more on tests between UPLs 0.8 and 0.9 V in order to determine where little or no oxide layer is formed. Further research into which catalyst characteristics affect the formation of Pt oxide would also be of interest. It is possible to implement voltage clipping at the LPL as well in order to further reduce degradation. In this regard, a suggestion is to examine the LPLs 0.5, 0.6, and 0.7 V. By combining the information regarding where the least degradation occurs for the UPL and LPL, a precise operating window can be determined that will increase the durability of the fuel cell.

Bibliography

- [1] Unfccc. ADOPTION OF THE PARIS AGREEMENT - Paris Agreement text English. Technical report.
- [2] Kai Sundmacher. *Advances in Chemical Engineering Fuel Cell Engineering*, volume 41. Elsevier, Amsterdam, 1 edition, 2012. ISBN 9780123868749.
- [3] Frank Barbir. *PEM Fuel Cells Theory and Practice*. Elsevier, second edition, 2013. doi: 10.1016/B978-0-12-078142-3.X5000-9.
- [4] Michael M. Whiston, Inês L. Azevedo, Shawn Litster, Kate S. Whitefoot, Constantine Samaras, and Jay F. Whitacre. Expert assessments of the cost and expected future performance of proton exchange membrane fuel cells for vehicles. *Proceedings of the National Academy of Sciences of the United States of America*, 116(11):4899–4904, 2019. doi: 10.1073/pnas.1804221116.
- [5] Tsuyoshi Takahashi, Takuya Ikeda, Kazuya Murata, Osamu Hotaka, Shigeki Hasegawa, Yuya Tachikawa, Masamichi Nishihara, Junko Matsuda, Tatsumi Kitahara, Stephen M. Lyth, Akari Hayashi, and Kazunari Sasaki. Accelerated Durability Testing of Fuel Cell Stacks for Commercial Automotive Applications: A Case Study. *Journal of The Electrochemical Society*, 169(4):044523, 4 2022. doi: 10.1149/1945-7111/ac662d.
- [6] Subramaniam Jayabal, Govindarajan Saranya, Dongsheng Geng, Lu Yin Lin, and Xiangbo Meng. Insight into the correlation of Pt-support interactions with electrocatalytic activity and durability in fuel cells. *Journal of Materials Chemistry A*, 8(19):9420–9446, 5 2020. doi: 10.1039/d0ta01530j.
- [7] Congwei Qin, Jue Wang, Daijun Yang, Bing Li, and Cunman Zhang. Proton exchange membrane fuel cell reversal: A review. *Catalysts*, 6(12), 12 2016. doi: 10.3390/catal6120197.
- [8] Brian T. Sneed, David A. Cullen, Kimberly S. Reeves, Ondrej E. Dyck, David A. Langlois, Rangachary Mukundan, Rodney L. Borup, and Karren L. More. 3D Analysis of Fuel Cell Electrocatalyst Degradation on Alternate Carbon Supports. *ACS Applied Materials and Interfaces*, 9(35):29839–29848, 9 2017. doi: 10.1021/acsami.7b09716.
- [9] Nagappan Ramaswamy, Swami Kumaraguru, Roland Koestner, Timothy Fuller, Wenbin Gu, Nancy Kariuki, Deborah Myers, Peter J. Dudenas, and Ahmet Kusoglu. Editors’ Choice—Ionomer Side Chain Length and Equivalent Weight Impact on High Current Density Transport Resistances in PEMFC

- Cathodes. *Journal of The Electrochemical Society*, 168(2):024518, 2 2021. doi: 10.1149/1945-7111/abe5eb.
- [10] Josef C. Meier, Carolina Galeano, Ioannis Katsounaros, Jonathon Witte, Hans J. Bongard, Angel A. Topalov, Claudio Baldizzone, Stefano Mezzavilla, Ferdi Schüth, and Karl J.J. Mayrhofer. Design criteria for stable Pt/C fuel cell catalysts. *Beilstein Journal of Nanotechnology*, 5(1):44–67, 2014. doi: 10.3762/bjnano.5.5.
- [11] Adam Riese, Dustin Banham, Siyu Ye, and Xueliang Sun. Accelerated Stress Testing by Rotating Disk Electrode for Carbon Corrosion in Fuel Cell Catalyst Supports. *Journal of The Electrochemical Society*, 162(7):F783–F788, 2015. doi: 10.1149/2.0911507jes.
- [12] Peng Ren, Pucheng Pei, Yuehua Li, Ziyao Wu, Dongfang Chen, and Shangwei Huang. Degradation mechanisms of proton exchange membrane fuel cell under typical automotive operating conditions. *Progress in Energy and Combustion Science*, 80, 9 2020. doi: 10.1016/j.pecs.2020.100859.
- [13] Angel A. Topalov, Serhiy Cherevko, Aleksandar R. Zeradjanin, Josef C. Meier, Ioannis Katsounaros, and Karl J.J. Mayrhofer. Towards a comprehensive understanding of platinum dissolution in acidic media. *Chemical Science*, 5(2): 631–638, 2 2014. doi: 10.1039/c3sc52411f.
- [14] Liyan Xing, M. Akhtar Hossain, Min Tian, Diane Beauchemin, Kev T. Adjemian, and Gregory Jerkiewicz. Platinum Electro-dissolution in Acidic Media upon Potential Cycling. *Electrocatalysis*, 5(1):96–112, 1 2014. doi: 10.1007/s12678-013-0167-9.
- [15] Rodney L. Borup, Ahmet Kusoglu, Kenneth C. Neyerlin, Rangachary Mukundan, Rajesh K. Ahluwalia, David A. Cullen, Karren L. More, Adam Z. Weber, and Deborah J. Myers. Recent developments in catalyst-related PEM fuel cell durability. *Current Opinion in Electrochemistry*, 21:192–200, 6 2020. doi: 10.1016/j.coelec.2020.02.007.
- [16] Jozsef Speder, Lena Altmann, Marcus Bäumer, Jacob J.K. Kirkensgaard, Kell Mortensen, and Matthias Arenz. The particle proximity effect: From model to high surface area fuel cell catalysts. *RSC Advances*, 4(29):14971–14978, 2014. doi: 10.1039/c4ra00261j.
- [17] Daniel J. S. Sandbeck, Niklas Mørch Secher, Masanori Inaba, Jonathan Quinson, Jakob Ejler Sørensen, Jakob Kibsgaard, Alessandro Zana, Francesco Bizzotto, Florian D. Speck, Michael T. Y. Paul, Alexandra Dworzak, Carsten Dosche, Mehtap Oezaslan, Ib Chorkendorff, Matthias Arenz, and Serhiy Cherevko. The Dissolution Dilemma for Low Pt Loading Polymer Electrolyte Membrane Fuel Cell Catalysts. *Journal of The Electrochemical Society*, 167(16):164501, 12 2020. doi: 10.1149/1945-7111/abc767.
- [18] Masanori Inaba, Alessandro Zana, Jonathan Quinson, Francesco Bizzotto, Carsten Dosche, Alexandra Dworzak, Mehtap Oezaslan, Søren Bredmose Simonsen, Luise Theil Kuhn, and Matthias Arenz. The Oxygen Reduction Reac-

- tion on Pt: Why Particle Size and Interparticle Distance Matter. *ACS Catalysis*, 11(12):7144–7153, 6 2021. doi: 10.1021/acscatal.1c00652.
- [19] Elliot Padgett, Venkata Yarlagadda, Megan E. Holtz, Matthew Ko, Barnaby D. A. Levin, Ratandeeep Singh Kukreja, Joseph M. Ziegelbauer, Ross N. Andrews, Jan Ilavsky, Anusorn Kongkanand, and David A. Muller. Mitigation of PEM Fuel Cell Catalyst Degradation with Porous Carbon Supports. *Journal of The Electrochemical Society*, 166(4):F198–F207, 2019. doi: 10.1149/2.0371904jes.
- [20] Matthias Arenz and Alessandro Zana. Fuel cell catalyst degradation: Identical location electron microscopy and related methods. *Nano Energy*, 29:299–313, 11 2016. doi: 10.1016/j.nanoen.2016.04.027.
- [21] Konrad Ehelebe, Nicolai Schmitt, Gustav Sievers, Anders W. Jensen, Armin Hrnjić, Pablo Collantes Jiménez, Pascal Kaiser, Moritz Geuß, Yu Ping Ku, Primož Jovanovič, Karl J.J. Mayrhofer, Bastian Etzold, Nejc Hodnik, María Escudero-Escribano, Matthias Arenz, and Serhiy Cherevko. Benchmarking Fuel Cell Electrocatalysts Using Gas Diffusion Electrodes: Inter-lab Comparison and Best Practices. *ACS Energy Letters*, 7(2):816–826, 2 2022. doi: 10.1021/acsenergylett.1c02659.
- [22] Jianlu Zhang and Jiujun Zhang. *Catalyst Layer/MEA Performance Evaluation*. Springer London, London, 2008. doi: 10.1007/978-1-84800-936-3.
- [23] Carl H Hamann, Andrew Hamnett, and Wolf Vielstich. *Electrochemistry 2. ed.* Wiley, 2007.
- [24] Mathan Chandran, Karthikeyan Palaniswamy, N. B. Karthik Babu, and Oisik Das. A study of the influence of current ramp rate on the performance of polymer electrolyte membrane fuel cell. *Scientific Reports*, 12(1), 12 2022. doi: 10.1038/s41598-022-25037-0.
- [25] Department of Energy (DOE) Durability Working Group. Rotating Disk-Electrode Aqueous Electrolyte Accelerated Stress Tests for PGM Electrocatalyst/Support Durability Evaluation DOE Durability Working Group 10/4/2011 Conditions Electrolyte: 0.1 to 1.0 M HClO₄ or 0.5 M H₂SO₄ (see Appendix A for discussion of effect of electrolyte). Technical report, 2011.
- [26] Masanobu Uchimura and Shyam S. Kocha. The Impact of Cycle Profile on PEMFC Durability. *ECS Transactions*, 11(1):1215–1226, 9 2007. doi: 10.1149/1.2781035.
- [27] Atsushi Ohma, Kazuhiko Shinohara, Akihiro Iiyama, Toshihiko Yoshida, and Akimasa Daimaru. Membrane and Catalyst Performance Targets for Automotive Fuel Cells by FCCJ Membrane, Catalyst, MEA WG. *ECS Transactions*, 41(1):775–784, 10 2011. doi: 10.1149/1.3635611.
- [28] Raghunandan Sharma and Shuang Ma Andersen. An opinion on catalyst degradation mechanisms during catalyst support focused accelerated stress test

- (AST) for proton exchange membrane fuel cells (PEMFCs). *Applied Catalysis B: Environmental*, 239:636–643, 12 2018. doi: 10.1016/j.apcatb.2018.08.045.
- [29] Yuanliang Zhang, Siguo Chen, Yao Wang, Wei Ding, Rui Wu, Li Li, Xueqiang Qi, and Zidong Wei. Study of the degradation mechanisms of carbon-supported platinum fuel cells catalyst via different accelerated stress test. *Journal of Power Sources*, 273:62–69, 1 2015. doi: 10.1016/j.jpowsour.2014.09.012.
- [30] Shima Alinejad, Masanori Inaba, Johanna Schröder, Jia Du, Jonathan Quinson, Alessandro Zana, and Matthias Arenz. Testing FC catalysts under more realistic reaction conditions: ASTs in gas diffusion electrode setup. *J. Phys. Energy* 2, 2020. doi: 10.1088/2515-7655/ab67e2.
- [31] Angel A. Topalov, Ioannis Katsounaros, Michael Auinger, Serhiy Cherevko, Josef C. Meier, Sebastian O. Klemm, and Karl J.J. Mayrhofer. Dissolution of platinum: Limits for the deployment of electrochemical energy conversion? *Angewandte Chemie - International Edition*, 51(50):12613–12615, 12 2012. doi: 10.1002/anie.201207256.
- [32] Yannick Garsany, Junjie Ge, Jean St-Pierre, Richard Rocheleau, and Karen E. Swider-Lyons. Analytical Procedure for Accurate Comparison of Rotating Disk Electrode Results for the Oxygen Reduction Activity of Pt/C. *Journal of The Electrochemical Society*, 161(5):F628–F640, 2014. doi: 10.1149/2.036405jes.

A

Appendix 1

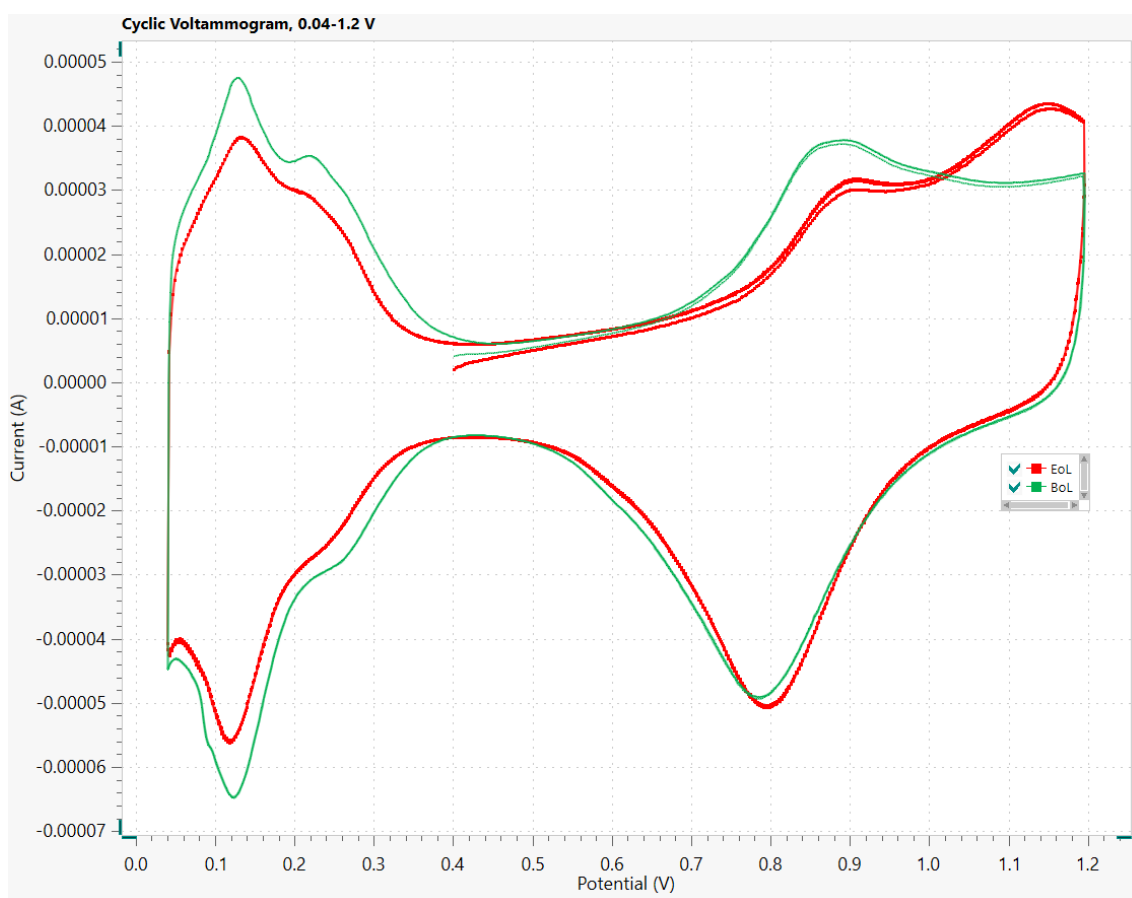


Figure A.1: Cyclic voltammogram current (A) over Potential (V) for catalyst C ink 5, 0.04-1.2 V with a scan rate of 20 mV/s. Green is the cyclic voltammogram at time 0 h and red is at time 17.78 h. There is an increase in the anodic scan in the interval 1.0 to 1.2 V. The cause is unknown.

DEPARTMENT OF PHYSICS
CHALMERS UNIVERSITY OF TECHNOLOGY
Gothenburg, Sweden
www.chalmers.se



CHALMERS
UNIVERSITY OF TECHNOLOGY